ALLEN INSTITUTE for NEURAL DYNAMICS

PREPRINT

Expansion-assisted selective plane illumination microscopy for nanoscale imaging of centimeter-scale tissues

Adam Glaser[1†*], Jayaram Chandrashekar[1†*], Sonya Vasquez[1], Cameron Arshadi[1], Rajvi Javeri[1], Naveen Ouellette[1], Xiaoyun Jiang[1], Judith Baka[1], Gabor Kovacs[1], Micah Woodard[1], Sharmishtaa Seshamani[1], Kevin Cao[1], Nathan Clack[2], Andrew Recknagel[1], Anna Grim[1], Pooja Balaram[3], Emily Turschak[3], Marcus Hooper[3], Alan Liddell[2], John Rohde[1], Ayana Hellevik[3], Kevin Takasaki[3], Lindsey Erion Barner[1], Molly Logsdon[1], Chris Chronopoulos[1], Saskia de Vries[1], Jonathan Ting[3], Steve Perlmutter[4], Brian Kalmbach[3], Nikolai Dembrow[3], Bosiljka Tasic[3], R. Clay Reid[3], David Feng[1], and Karel Svoboda[1]

[1]Allen Institute for Neural Dynamics, Seattle, WA
[2]Chan Zuckerberg Initiative, Redwood City, CA
[3]Allen Institute for Brain Science, Seattle, WA
[4]University of Washington, Seattle, WA

†Equal contributors.
*Correspondence: adam.glaser@alleninstitute.org; jayaramc@alleninstitute.org

Abstract

Recent advances in tissue processing, labeling, and fluorescence microscopy are providing unprecedented views of the structure of cells and tissues at sub-diffraction resolutions and near single molecule sensitivity, driving discoveries in diverse fields of biology, including neuroscience. Biological tissue is organized over scales of nanometers to centimeters. Harnessing molecular imaging across intact, three-dimensional samples on this scale requires new types of microscopes with larger fields of view and working distance, as well as higher throughput. We present a new expansion-assisted selective plane illumination microscope (ExA-SPIM) with aberration-free 1.5 µm×1.5 µm×3 µm optical resolution over a large field of view (10.6×8.0 mm^2) and working distance (35 mm) at speeds up to 946 megavoxels/sec. Combined with new tissue clearing and expansion methods, the microscope allows imaging centimeter-scale samples with 375 nm lateral and 750 nm axial resolution (4× expansion), including entire mouse brains, with high contrast and without sectioning. We illustrate ExA-SPIM by reconstructing individual neurons across the mouse brain, imaging cortico-spinal neurons in the macaque motor cortex, and visualizing axons in human white matter.

Keywords: selective plane illumination microscopy, light-sheet microscopy, tissue clearing, expansion microscopy, large-scale imaging

Introduction

Biological tissue is organized over scales of nanometers to centimeters. Understanding individual cells and multicellular organization requires probing the architecture of tissue over these spatial scales simultaneously. However, standard microscope objectives with high resolutions have limited working distances (<1 mm) and fields of view (<1 mm). Imaging large tissue volumes at high resolutions therefore requires physical sectioning and extensive tiling. Physical sectioning distorts the imaged tissue and focal planes have optical distortions at the edges of the field of view (Zhang & Gross 2019). These factors complicate stitching across sections and tile boundaries at sub-micrometer resolutions which in turn increases the complexity and cost of downstream image analysis.

Because light aberration and scattering limits high-resolution microscopy in tissue, including two-photon microscopy, to depths of hundreds of micrometers, sectioning and tiling have traditionally been viewed as necessary to image large specimens (Portera-Cailliau et al. 2005; Tsai et al. 2009; Oh et al. 2014; Economo et al. 2016). However, advances in histological methods, including clearing (Richardson & Lichtman 2015; Spalteholz 1914; Dodt et al. 2007; Tsai et al. 2009; Hama et al. 2011; Becker et al. 2012; Ertürk et al. 2012; Chung & Deisseroth 2013; Ke et al. 2013; Susaki et al. 2014; Tainaka et al. 2014; Yang et al. 2014; Renier et al. 2014; Hou et al. 2015;

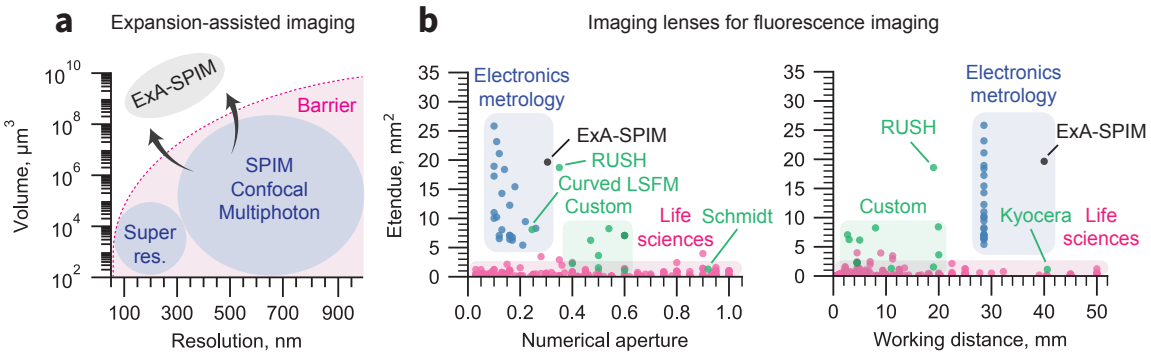

Figure 1: Breaking the volumetric imaging barrier. **(a)** Current fluorescence microscopy approaches are bounded by a volumetric imaging barrier (thick pink line; inspired by (Daetwyler & Fiolka 2023)). Resolution is limited by the diffraction limit. The accessible imaging volume is limited by specifications of life sciences microscope objectives. The former can be surpassed by using tissue expansion, and the latter can be overcome by using highly engineered lenses from the electronics metrology industry. **(b)** The etendue (G) of 90% of life sciences objectives (magenta) are are <1 mm^2 (Yueqian & Herbert 2019), apart from several custom lenses (green). In contrast, lenses developed for electronics metrology can have G > 10 mm^2. The lens used in the ExA-SPIM system provides a field of view of 16.8 mm^2 with NA = 0.305 (G = 19.65 mm^2). This etendue is comparable to the custom RUSH objective (Fan et al. 2019), but with twice the working distance and correction for liquid media. The RUSH, Schmidt (Voigt et al. 2024), Kyocera[a], and large etendue curved focal plane (Tang et al. 2024) lenses that lie outside of their colored zone are highlighted.

a. https://www.ksoc.co.jp/en/seihin/immersion-objective/immersion-objective.html

Costantini et al. 2015; AU - Chi et al. 2018) and expansion for microscopy (ExM) (Chen et al. 2015; Chen et al. 2016; Chozinski et al. 2016; Ku et al. 2016), now promise diffraction-limited imaging deep in tissue. Avoiding sectioning and reducing tiling requires overcoming the "volumetric" imaging barrier of microscopy (i.e., the maximum volume that may be imaged) (**Figure 1a**). Expansion up to 20× has been demonstrated (Chang et al. 2017), which provides access to molecular spatial scales (10's of nm), approaching those of cryo electron microscopy (a few nm) (Cheng et al. 2015; Fernandez-Leiro & Scheres 2016; Nogales & Scheres 2015). These ExM methods produce large, fragile three-dimensional samples, further emphasizing the need for overcoming the volumetric imaging barrier.

We combine a new microscope and methods for tissue clearing and expansion, which we jointly refer to as Expansion-Assisted Selective Plane Illumination Microscopy (ExA-SPIM). Unlike expansion lattice light-sheet microscopy, (G. Gao et al. 2023) which is limited to small tissue volumes « 1 mm^3, ExA-SPIM works with expansion of large centimeter-scale tissue volumes, such as the mouse brain. Leveraging optics and detectors developed for the electronics metrology industry, ExA-SPIM has a field of view ~100× larger (13.3 mm diameter) and a working distance ~10× larger (35 mm) compared to objectives typically used for biological microscopy, while retaining a relatively high numerical aperture (NA) = 0.305. When combined with 3× expansion the system achieves an effective resolution of ~0.5 µm laterally, and ~1 µm axially, at imaging speeds of up to 946 megavoxels/sec. Imaging with diffraction-limited resolution throughout centimeter-scale specimens requires tissue samples with small index of refraction variations (Weiss et al. 2021). To achieve this goal, we developed a novel expansion method for centimeter-scale tissue samples. Tailoring the expansion factor allows fine tuning the effective resolution for specific tissue types and scientific questions.

We apply ExA-SPIM to imaging and reconstructing mammalian neurons. Axonal arbors of individual neurons are complex, branched structures that transmit electrical impulses over distances of centimeters, yet axons can be thinner than 100 nm (Economo et al. 2016; Winnubst et al. 2019). Axons contain numerous varicosities that make synapses with other neurons. Tracing the axonal arbors of single neurons is critical to define how signals are routed within the brain and is also necessary for classifying diverse neuron types into distinct types (Economo et al. 2016; Wang et al. 2021; Winnubst et al. 2019; Xu et al. 2021; Zhang et al. 2021). Large-scale projects based on single cell transcriptomics in the mouse and human brain have revealed a great diversity of neuron types (Hodge et al. 2019; Tasic et al. 2018; Zizhen Yao et al. 2023). However, the throughput of neuronal reconstructions has remained too

low for single neuron reconstructions on a comparable scale, even in mice. Throughput is limited in part by speed and image quality of existing microscopy methods. We demonstrate that ExA-SPIM provides high-resolution fluorescence microscopy over teravoxel image volumes with minimal distortions, and thereby enables brain-wide imaging with high contrast, resolution, and speed.

Results

We first describe the microscope optics and how they overcome specific requirements for multi-scale tissue imaging. We then outline a new histological method for clearing and expanding centimeter-scale specimens, although details are relegated to extensive protocols ((Ouellette et al. 2023), dx.doi.org/10.17504/protocols.io.n92ldpwjxl5b/v1). Finally, we illustrate ExA-SPIM performance for imaging neurons in whole mouse brains and large samples of non-human primate and human cortex.

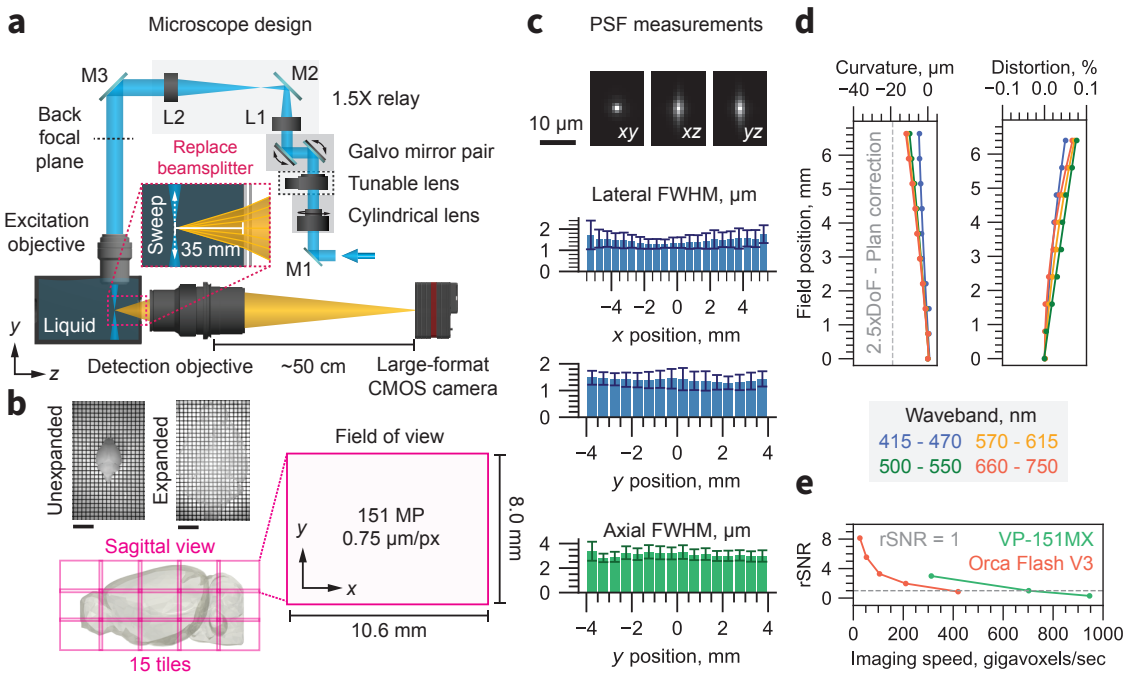

Figure 2: Microscope overview. (a) Schematic of the ExA-SPIM system. Light enters the system from the laser combiner and is reflected by mirror M1. A cylindrical lens focuses the light in one dimension onto the surface of a tunable lens, which is magnified onto the back focal plane of the excitation through a 1.5× relay consisting of lenses L1 and L2 and mirrors M2 and M3. The excitation objective is oriented vertically and dipped into a liquid immersion chamber. The tunable lens is conjugated to the back focal plane of the excitation objective to enable axial sweeping. A pair of galvo mirrors are used in tandem to translate the position of the light sheet in *z* (along the optical axis of the detection objective). The detection objective is oriented horizontally. A beam splitter is removed from the lens and replaced with approximately 35 mm of water. A large-format CMOS camera captures images from the detection lens, at a back focusing distance of 50 cm. **(b)** The field of view of the system is 10.6×8.0 mm (13.3 mm diagonal), which is digitized by the camera into a 151-megapixel (MP) image with 0.75 µm/px sampling. Although the optical resolution of the detection lens is ~1.0 µm, the sampling limited resolution based on the Nyquist criterion is ~1.5 µm. The large field of view dramatically reduces the need for tiling. For example, a 3× expanded mouse brain can be captured in only 15 tiles. Representative images of a 3 expanded mouse brain are shown with a 1 cm scale bar. **(c)** The PSF for 561 nm excitation is shown in the *xy*, *xz*, and *yz* planes. The mean and standard deviation of the lateral and axial full-width half-maximum are shown as a function of *x* and *y* position across the full field of view. **(d)** The field curvature and distortion of the system as a function of field position is shown for different wavebands. The field curvature is <2.5× the depth of field (DoF) for all wavebands. This performance is better than "Plan" specified life sciences objectives (Yueqian & Herbert 2019). **(e)** The relative signal-to-noise-ratio (rSNR) of the VP-151MX CMOS camera and an Orca Flash V3 sCMOS camera as a function of imaging speed. The VP-151MX camera provides equivalent SNR at nearly twice the imaging speed.

ExA-SPIM microscope

The ideal fluorescence microscope for large-scale tissue imaging would provide: (1) nanoscale resolution, (2) over centimeter-scale volumes, (3) with minimal tiling and sectioning, (4) high isotropy in resolution and contrast, and (5) fast imaging speed. Multiple imaging systems have been developed within this space, each with unique advantages but inevitable trade-offs (Huisken et al. 2004; Dodt et al. 2007; Wu et al. 2013; Kumar et al. 2014; Tomer et al. 2014; Economo et al. 2016; Narasimhan et al. 2017; Power & Huisken 2017; Migliori et al. 2018; Chakraborty et al. 2019; Voigt et al. 2019; Voleti et al. 2019; Y. Chen et al. 2020; D. Chen et al. 2020; Glaser et al. 2022; Wang et al. 2021; Xu et al. 2021; Zhang et al. 2021; Xiaoli Qi et al. 2023; Vladimirov et al. 2024).

The choice of microscope objective is a critical design choice. Microscope objectives impose trade-offs between the smallest objects that can be resolved (i.e., the resolution), how much of the specimen can be observed at once (i.e., the field of view), and how thick of a specimen may be imaged (i.e., the working distance). These trade-offs are not based on physical law, but reflect limitations of optical design, engineering, and lens manufacturing.

The trade-off between resolution and field of view is related to the etendue (G), which is proportional to the number of resolution elements of an optical system. The etendue is a quadratic function of the lens field of view (FOV) and numerical aperture (NA).

$$G = \frac{\pi}{4}(FOV \times NA)^2 \tag{1}$$

Similarly, for a given NA, the required lens diameter increases proportionally with the required working distance (WD). The ideal lens for large-scale volumetric microscopy would provide large G and WD values.

90% of commercially available objectives for biological microscopy have G < 1 mm^2 (Yueqian & Herbert 2019), and the vast majority of commercially available lenses have lens diameters <2 cm. Several attempts have been made to develop custom lenses for specific applications. The 'Mesolens' provides an etendue of G = 6.25 mm^2, with a FOV = 6 mm, NA = 0.47, and WD = 3 mm (McConnell et al. 2016), but difficulties with manufacturing has limited adoption (McConnell 2020). An objective with an etendue of G = 7.07 mm^2, FOV = 5 mm, NA = 0.6, and WD = 2.7 mm has been developed for two-photon microscopy *in vivo* (Sofroniew et al. 2016). However, this lens is customized for infrared illumination and exhibits significant field curvature. Additional custom lenses have subsequently been developed for two-photon microscopy, although none of these lenses are suitable for large-scale fluorescence microscopy (Keisuke Ota et al. 2020; Rumyantsev et al. 2020; Yu et al. 2021). A custom lens with a large etendue of G = 18.86 mm^2, FOV = 14 mm, NA = 0.35, and WD = 19 mm has been developed for the real-time ultra-large-scale high-resolution (RUSH) microscope (Fan et al. 2019). Despite the large etendue, the lens is not commercially available and not designed for immersion, which is critical for imaging cleared or expanded tissues. Custom lenses such as the Schmidt (Voigt et al. 2024), Cousa (Yu et al. 2024), and Kyocera[1] lenses offer long working distances but small etendues.

Rather than designing a highly customized lens from scratch, we leveraged engineering investments that have been made in a different domain. High-resolution, high-speed imaging is widely used within the machine vision and metrology industry, where optical microscopes are used to map defects in semiconductors and other electronic devices. As the physical size of electronic components (e.g., pixels on flat panel displays) have become smaller, lenses for this domain have been designed with increasing NA, accessing biologically relevant resolutions (<1 μm). For a given NA these lenses have remarkably large field of views (and thus high etendues), low field curvature, minimal distortion, and chromatic correction throughout the visible wavelengths. A comparison of the etendue as a function of NA and working distance for these lenses, and commercial and custom life sciences lenses is summarized in (**Figure 1b**). A more detailed summary of many electronics metrology technologies[2,3,4,5] is provided as **Supplementary Data**. Despite their superb specifications, both the lenses and camera sensors are readily available, are manufactured in large quantities, and are cost effective. We investigated the performance of metrology optics and cameras for imaging biological tissues and adapted a particular set of machine vision optics for biological microscopy.

The detection path of the system uses a lens[6] with 5.0× magnification, with diffraction-limited imaging at NA

1. https://www.ksoc.co.jp/en/seihin/immersion-objective/immersion-objective.html
2. https://schneiderkreuznach.com/en/industrial-optics/lenses/line-scan-lenses/diamond
3. https://www.excelitas.com/product/dfine-hr-24128-lens
4. https://navitar.com/products/imaging-optics/singleshot/
5. https://www.nikon.com/business/industrial-lenses/
6. https://vision.vieworks.com/en/lens/veo_jm/VEO_JM_DIAMOND_5.0X_F1.3

= 0.305, and a 16.8 mm field of view (G = 19.65 mm^2) (VEO_JM DIAMOND 5.0×/F1.3, Schneider-Kreuznach, Germany) (**Figure 2a**). A 35 mm thick glass beam splitter, normally used for co-axial illumination, is replaced with an optically equivalent thickness of liquid media. This enables spherical aberration free imaging through 35 - 40 mm of liquid media (tunable for refractive indices between 1.33 - 1.56), including expanded hydrogels and cleared tissues. The lens is paired with a large-format CMOS sensor[7] (VP-151MX, Vieworks Korea), based on the Sony IMX411 sensor[8], with a single-sided rolling shutter, 151 megapixels, 14192 (H) × 10640 (V), and a pitch of 3.76 µm. The camera captures a field of view of 10.6×8.0 mm (13.3 mm diagonal), capable of covering an entire 3× expanded mouse brain in only 15 tiles (**Figure 2b**). A conventional SPIM system would require 400+ tiles to image an entire cleared brain at equivalent resolutions (**Figure 1 Supplementary Figure 1**). A comparison of the selected lens and camera sensor with a state-of-the-art cleared tissue objective lens (Nikon 20× GLYC) and sCMOS camera (Hamamatsu Orca BT-Fusion) are shown in **Figure 1 Supplementary Figure 2**.

To improve axial resolution, our system synchronizes an axially-swept light-sheet with the rolling shutter of the Sony IMX411 sensor (Dean et al. 2015). The CMOS sensor parallelizes readout across 14192 pixels per row, thereby achieving equivalent or greater pixel rates than typical scientific CMOS (sCMOS) sensors, even with an increased time per line and a relatively low frame rate (<6.4 Hz). As a result, the ExA-SPIM microscope operates at a higher imaging speed with comparable signal-to-noise ratio (SNR) to sCMOS-based systems (**Figure 2e**). The low frame rate of the sensor facilitates accurate axially swept imaging using generic scanning hardware at an imaging speed of 946 megavoxels/sec. The excitation lens (1-290419, Navitar) is infinity-corrected (to enable axially swept excitation) and provides diffraction-limited resolution at NA = 0.133 over a 16 mm field of view. When fitted with a custom dipping cap, the excitation lens provides a working distance of 53 mm in water. The beam shaping in the excitation path is configured to deliver a light sheet with NA = 0.10 and width of 12.5 mm (full-width half-maximum).

Based on these lenses, and the travel limits of a mechanical motorized stage, the ExA-SPIM is capable of imaging a 200×52×35 mm^3 volume, with ~1.5 µm lateral and ~3 µm axial native optical resolution, and minimal field curvature [quantified using the methodology described in (Vladimirov et al. 2024)] and distortion (**Figure 2c-d**). We leveraged this large volume to image intact, expanded tissues. The expansion factor allows tuning the effective resolution for specific biological applications.

With 3× tissue expansion, the system can image a native tissue volume of 67×17×12 mm^3 with an effective optical resolution of ~0.5 µm laterally and ~1 µm axially. This amounts to >100 teravoxels, which can be captured without the need for physical sectioning and with minimal tiling. A summary plot comparing the focal volume, isotropy, and imaging speed of our new ExA-SPIM system to other large-scale volumetric imaging systems is shown in **Figure 1 Supplementary Figure 3**. Individual data points are listed in **Table S2**.

The large-scale and high-speed imaging made possible by the ExA-SPIM system required new software for controlling the microscope, as well as downstream computational pipelines for compressing and handling the resulting datasets. We developed custom acquisition software capable of interfacing with the VP-151MX camera driver (https://github.com/acquire-project), which streams imaging data directly to next-generation file formats (Beati et al. 2020; Clack et al. 2023; Moore et al. 2021). Using a combination of high-speed networking, fast on-premises storage[9], and real-time compression, our current imaging pipeline enables a throughput to cloud storage of >100 TB per day, using commodity hardware. This pipeline is actively being developed, with ongoing efforts focused on standardizing every processing step around the OME-Zarr file format(Moore et al. 2023).

Whole-brain expansion

Tissue expansion for microscopy (ExM) enables imaging specimens at effective resolutions well below the diffraction limit of light microscopes (Chang et al. 2017; Chen et al. 2015; Tillberg & Chen 2019). Moreover, ExM can produce optically clear specimens with low fluorescence background. Multiple ExM variations have emerged, driven by specific biological questions. These include engineered hydrogel chemistry for post expansion molecular interrogation of proteins or RNA (Asano et al. 2018; Cho & Chang 2022; Tillberg et al. 2016; Yi Cui et al. 2022), formulations that provide gel stiffness (R. Chen et al. 2021) or tunable expansion up to >10× (Damstra et al. 2022; Klimas et al. 2023; Sarkar et al. 2022; Truckenbrodt et al. 2018). Most of these protocols have been developed for

7. https://vision.vieworks.com/en/camera/area_scan/VP_series
8. https://www.sony-semicon.com/files/62/pdf/p-13_IMX411ALR_AQR_Flyer.pdf
9. https://vastdata.com/

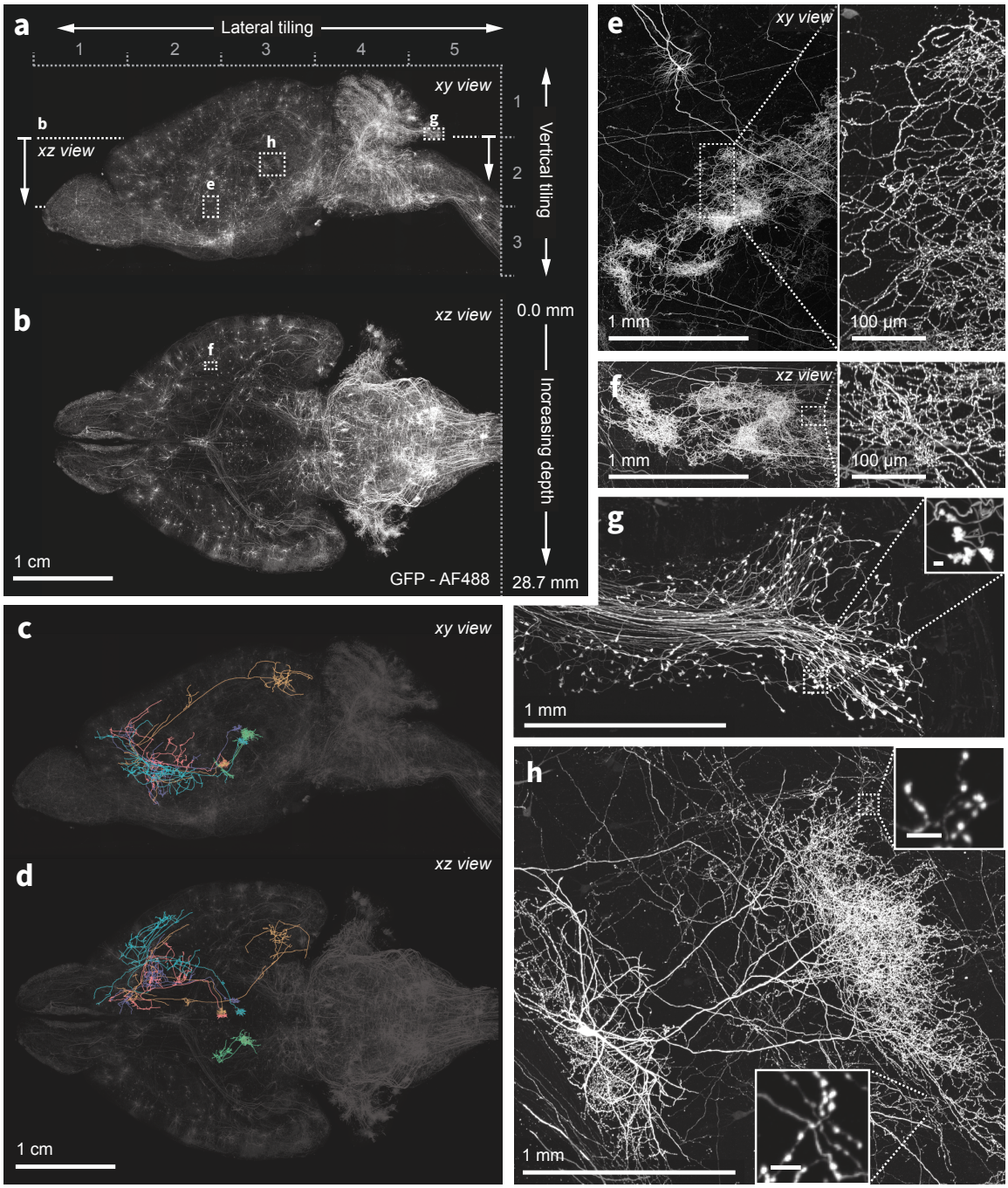

Figure 3: Nanoscale imaging of intact mouse brains. (a-b) Neurons in the mouse brain were labeled using a combination of PHP.eB pseudotyped enhancer AAV (pAAV-AiE2255m-minBG-iCre(R297T)-BGHpA that drives expression of a mutated iCre(R297T) recombinase and targets the 149 PVT-PT Ntrk1Glut molecular subclass in the whole mouse brain taxonomy (Zizhen Yao et al. 2023)) together with an AAV expressing GFP in a Cre-dependent manner. Sparse and bright labeling was achieved for neurons in the olfactory bulb, striatum, thalamus, midbrain and medulla. Intact mouse brains were expanded (3×) and imaged using the ExASPIM microscope ((Ouellette et al. 2023), dx.doi.org/10.17504/protocols.io.n92ldpwjxl5b/v1). **(c-d)** Representative reconstructions of complete axonal morphologies of 5 thalamic neurons. **(e-h)** ExA-SPIM imaging resolves dense axonal arbors and varicosities across various brain regions with high resolution and isotropy (Supplementary Videos 5-8). *xy* and *xz* views of a dense arbor in the striatum (e-f); mossy fiber axon terminals and boutons **(g)**; an individual hippocampal CA3 neuron and its extensive local axons **(h)**. Images are displayed as maximum intensity projections and inset scale bars correspond to 10 m post tissue expansion unless otherwise specified.

specimens that are at most 100's of micrometers thick. We developed ExM methods for centimeter-scale tissue samples, including entire mouse brains. A key requirement for ExA-SPIM is optical clearing so that the entire volume can be imaged with diffraction-limited resolution without sectioning. Index of refraction inhomogeneities in heavily myelinated fiber tracts pose particular challenges. Clearing was achieved by stringent dehydration and delipidation prior to gelation and expansion. We systematically evaluated dehydration agents, including methanol, ethanol, and tetrahydrofuran (THF), followed by delipidation with commonly used protocols on 1 mm thick brain slices. Slices were expanded and examined for clarity under a macroscope. Dehydration using THF was followed by two sequential delipidation steps. First DISCO type clearing (AU - Chi et al. 2018; Renier et al. 2014) followed by aqueous delipidation ((Chen & Svoboda 2020), dx.doi.org/10.17504/protocols.io.zndf5a6) rendered the samples extremely transparent (**Figure 3a**) ((Ouellette et al. 2023), dx.doi.org/10.17504/protocols.io.n92ldpwjxl5b/v1). In addition to clearing specimens, delipidation facilitates immunolabeling brain samples prior to gelation and expansion (**Figure 3**). Signal amplification facilitates high contrast imaging of small structures, especially since the increase in volume upon expansion dilutes the concentration of the fluorophore. For gelation we used VA-044 as the initiator, instead of the more commonly used APS/TEMED (Tillberg & Chen 2019). VA-044 initiates free radicals at a temperature-dependent rate. At low temperatures (4°C) the gelling reagents are allowed to diffuse to the center of thick samples, followed by higher temperatures (37°C) to trigger uniform polymerization. Our protocol provides nearly isotropic expansion of the whole sample (including internal brain structures) (**Figure 3**). Although developed for the mouse brain, we have successfully used this protocol for other large specimens, such as a 1 cm×1 cm×1.5 cm piece of macaque motor cortex (**Figure 5**), as well as a 1 cm×1 cm×0.01 cm section of human visual cortex (**Figure 6**) ((Ouellette et al. 2023), dx.doi.org/10.17504/protocols.io.n92ldpwjxl5b/v1).

Imaging single neurons across entire mouse brains

We cleared and expanded entire mouse brains and imaged individual neurons, resolving their dense axonal projections (**Figure 3**). Tracking the axons of individual neurons is a challenging problem—axons collaterals can be very thin (<100 nm) and traverse large distances (centimeters), spanning vast areas of the brain. This requires high-resolution, high-contrast imaging of the entire brain without loss of data. Current best-in-class approaches (Economo et al. 2016; Gong et al. 2013; Gong et al. 2016; Winnubst et al. 2019) require physical sectioning and extensive tiling, which complicates downstream data processing. In addition, imaging lasts multiple days, which increases the chance for experimental failure and data loss. Finally, the resolution of these imaging methods is highly anisotropic (typically <1:6), which compromises the ability to perform unambiguous axon tracing.

We expressed GFP in a sparse subset of neurons in an enhancer virus mouse to label subcortical projection neurons. Brains were expanded (3×) and imaged in 15 tiles in as little as 24 hours. Because of the lack of physical tissue slicing, minimal tiling, and excellent performance of the microscope, datasets are aligned with an average residual error of <2 pixels between interest point correspondences in neighboring tiles (Hörl et al. 2019). Tile alignment of a representative dataset based on initial stage coordinates (**Supplementary Videos 1-2**), after stitching optimization (**Supplementary Videos 3**), and after fusion (**Supplementary Videos 4**) are available as **Supplementary Materials**. Dense axonal projections and varicosities are clearly visible (**Figure 3c-h**) and long-range axons can be tracked across the brain **Supplementary Videos 5-8**). The achromatic performance of the ExA-SPIM optics also enables multiple fluorescence channels to be acquired from mouse brains (e.g. GFP and tdTomato) (**Figure 4**).

Imaging cortico-spinal tract neuron in macaque motor cortex

We next established that our methods are applicable to larger brains. With minor adaptations, we applied our clearing and expansion protocol to a 1 cm×1 cm×1.5 cm block of pigtail macaque brain from the hand-wrist and trunk regions of primary motor cortex. Due to its strong myelination, this region of the primate brain is particularly difficult to clear and image (Van Essen et al. 2019). The specimen contained cortico-spinal neurons expressing a fluorescent protein (tdTomato) driven by retrograde AAV injected into the intermediate and ventral laminae of the cervical spinal cord. ExA-SPIM image volumes revealed brightly labeled cortico-spinal neurons (**Figure 5a-b** and **Supplementary Videos 9-11**). Individual neurons, their dendritic arbors, and extensive dendritic spines as well as the descending axon and collaterals are clearly discernible (**Figure 5c-f** and **Supplementary Video 12**). Additionally, even in down sampled data (~1 μm effective voxel size), we can follow axonal pathways. This raises the possibility that with a small number of slices (~6×1 cm thick slabs) and reduced imaging resolution, a

modified inverted (Wu et al. 2013; Kumar et al. 2014) or open-top (McGorty et al. 2015; Glaser et al. 2017; Glaser et al. 2019; Barner et al. 2020; Glaser et al. 2022) ExA-SPIM design (**Figure 4 Supplementary Figure 1**) could provide a mesoscale map of white matter axons across the entire macaque brain. A single brain could be imaged in ~4 days (**Table S3**). Existing efforts to map pathways in the primate brain at this resolution requires slicing the brain in 300 µm sections and laboriously assembling the resulting images into a coherent 3D volume (Xu et al. 2021).

Visualizing axons in human neocortex and white matter

Heavy chain neurofilaments comprise the internal scaffolds of long-range projection axons. Visualizing these neurofilaments with immunofluorescence could provide detailed information about axonal trajectories without the need for gene transfer methods, and which cannot be achieved with other methods, such as diffusion magnetic resonance imaging (Huang et al. 2021; Van Essen et al. 2019) or high-resolution optical coherence tomography (Tianqi Li et al. 2019). We next evaluated ExA-SPIM for imaging immunolabeled heavy chain neurofilaments in the human neocortex (**Figure 6**).

We cleared and expanded (4×) a ~1 cm×1 cm×0.01 cm piece of human neocortex (**Figure 6a**) and labeled the tissue with fluorescent SMI-32, which preferentially stains heavy chain neurofilaments. Individual axons and their trajectories are clearly visible through the 350 µm thick sample (**Figure 6b-d**). The larger axons (>1 µm) are well separated from each other in both the gray and white matter. In the white matter, axons are arranged as multiple

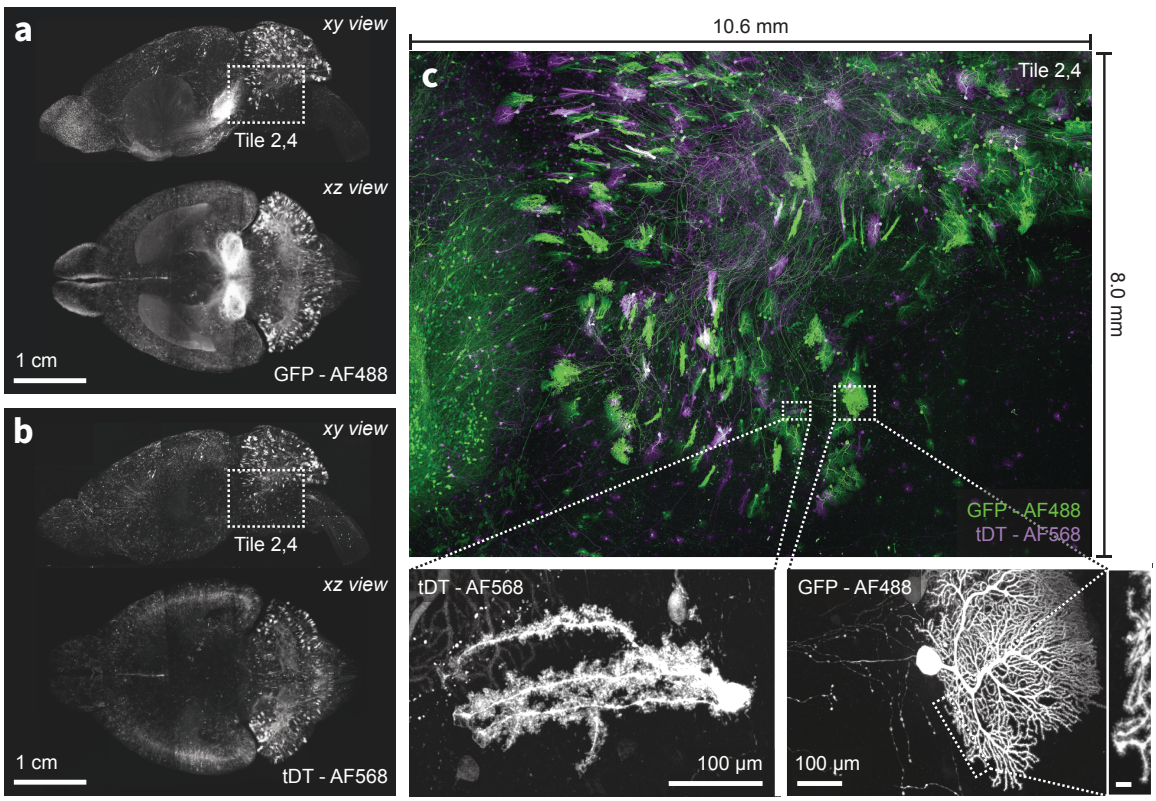

Figure 4: Multi-color imaging of centimeter-scale tissues with nanoscale resolution. (a-b) An intact mouse brains was expanded (3×) and sparsely labeled neurons expressing GFP and tdTomato were imaged using the ExA-SPIM microscope ((Ouellette et al. 2023), dx.doi.org/10.17504/protocols.io.n92ldpwjxl5b/v1). An overlay of both channels for a single tile is shown in **(c)**. The achromatic performance of the optics enabled diffraction-limited imaging in both color channels, as illustrated by the ability to resolve individual spines along the dendrites of Purkinje cells in the cerebellum. Images are displayed as maximum intensity projections and inset scale bars correspond to 10 µm post tissue expansion unless otherwise specified.

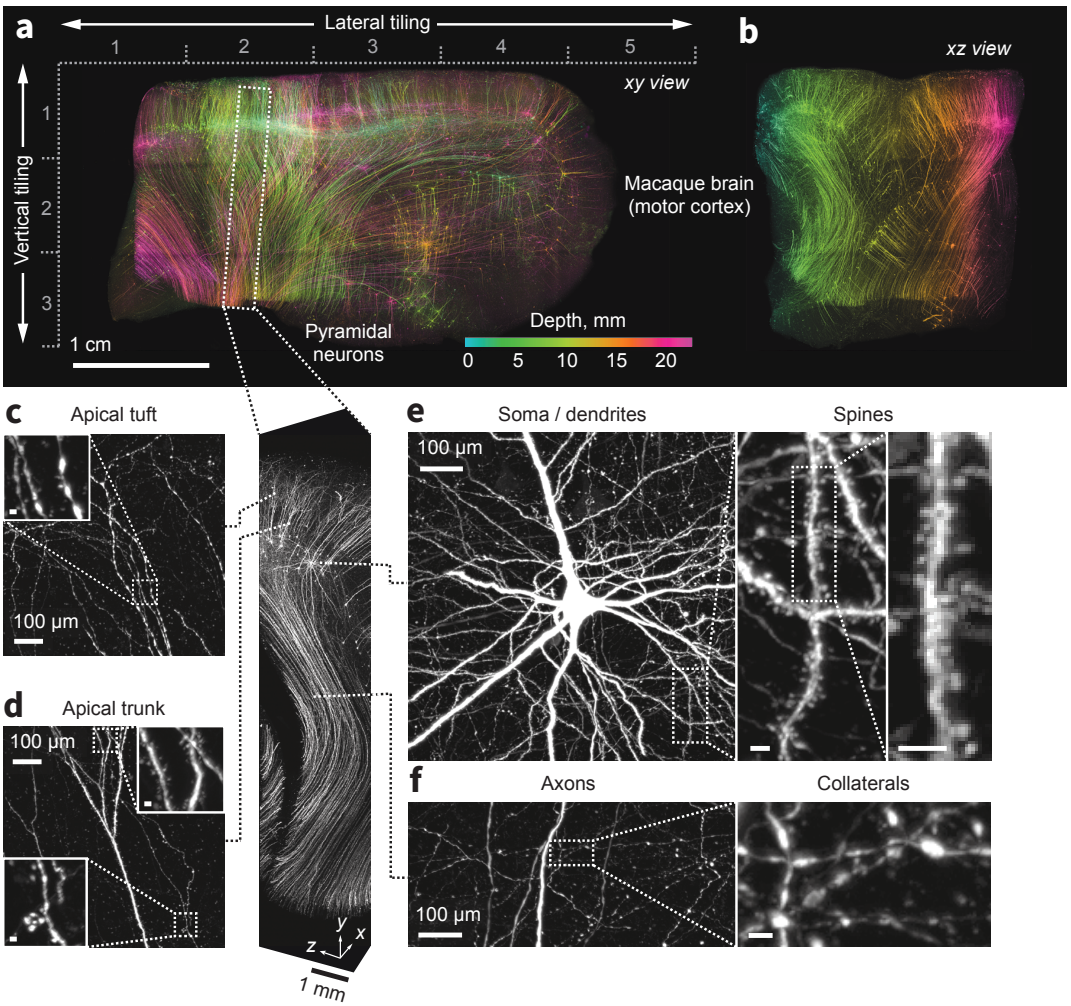

Figure 5: Expansion and imaging of a large volume of macaque brain. A 1 cm×1 cm×1.5 cm block of macaque primary motor cortex was expanded (3×) and imaged on the ExA-SPIM (**Supplementary Videos 9-11**). Corticospinal neurons were transduced by injecting tdTomato-expressing retro-AAV into the spinal cord. **(a-b)** Maximum intensity projections of the imaged volume pseudo colored by depth. The axes descriptors in **(a)** indicate the 5×3 tiling used to image this volume. **(c-f)** Fine axonal and dendritic structures including descending axons, collaterals and dendritic spines are clearly discernable in the images throughout the entire volume. See **Supplementary Video 12**. Images are displayed as maximum intensity projections with the following thicknesses: **(a)** 23 mm, **(b)** 45 mm, **(c-f)** 1 mm. Inset scale bars correspond to 10 µm post tissue expansion unless otherwise specified.

intercalated populations coursing in different directions, rather than as homogeneous fascicles. These results demonstrate the feasibility of using ExA-SPIM for visualizing white matter tract axons and lay the foundation for scaling this data acquisition to multiple, thick tissue sections, and ultimately the entire human brain.

Discussion

Recent breakthroughs in histological methods (Richardson & Lichtman 2015; Spalteholz 1914; Dodt et al. 2007; Tsai et al. 2009; Hama et al. 2011; Becker et al. 2012; Ertürk et al. 2012; Chung & Deisseroth 2013; Ke et al. 2013; Susaki et al. 2014; Tainaka et al. 2014; Yang et al. 2014; Renier et al. 2014; Hou et al. 2015; Costantini et al. 2015; AU - Chi et al. 2018), fluorescent labeling strategies (Kim et al. 2015; Susaki et al. 2020; Mao et al. 2020), fast and sensitive cameras, and new microscopes (Huisken et al. 2004; Dodt et al. 2007; Wu et al. 2013; Kumar et al. 2014; Tomer et al. 2014; Economo et al. 2016; Narasimhan et al. 2017; Power & Huisken 2017; Migliori et al. 2018;

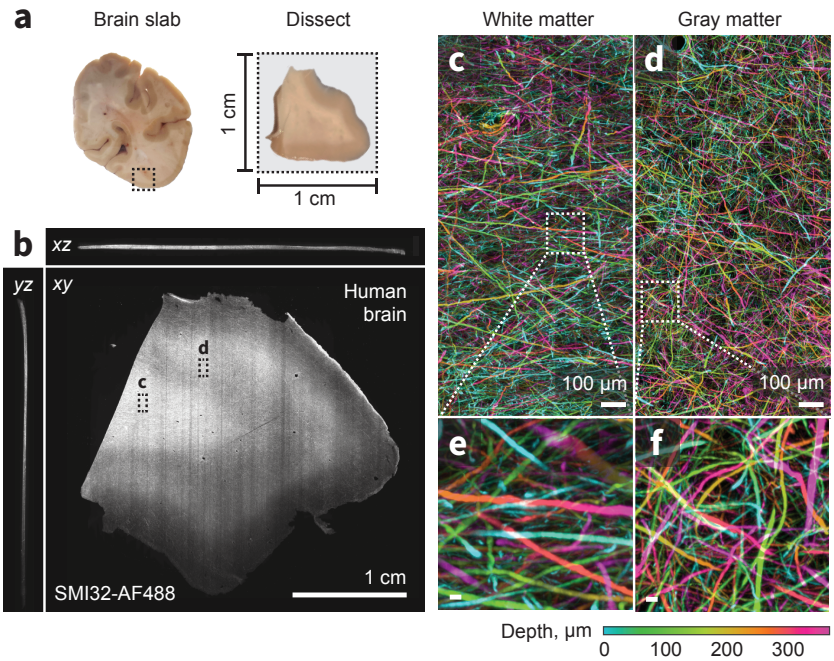

Figure 6: ExA-SPIM imaging of human tissue. (a-b) A region from the medial temporal-occipital cortex was manually dissected into a ~1 cm×1 cm block, which was subsequently sectioned into ~100 µm sections for tissue expansion (4×), labeling, and ExA-SPIM imaging. **(c-d)** Maximum intensity projection of a region of interest from white and gray matter, pseudo colored by depth. **(e-f)** Individual axons and their trajectories are clearly resolved with high contrast. Images are displayed as maximum intensity projections across 350 µm **(b-f)**. Inset scale bars correspond to 10 µm post tissue expansion unless otherwise specified.

Chakraborty et al. 2019; Glaser et al. 2019; Voigt et al. 2019; Voleti et al. 2019; Y. Chen et al. 2020; D. Chen et al. 2020; Wang et al. 2021; Xu et al. 2021; Zhang et al. 2021; Glaser et al. 2022; Xiaoli Qi et al. 2023; Vladimirov et al. 2024) are revolutionizing our ability to study the molecular organization of cells and tissues with fluorescence microscopy.

For many applications it is necessary to reconstruct tissues with high resolution and contrast over large spatial scales, including cells, organs, or even entire organisms. Such multi-scale imaging is necessary to reconstruct individual neurons in the mouse brain, which can span many millimeters, but with axons that are often less than 100 nm thick. ExA-SPIM addresses this need for imaging of large tissue volumes with high resolution and contrast. The resulting image volumes are sufficient for manual neuron tracing, and preliminary data suggests that automated segmentation of thin axons is improved compared to previous approaches (Winnubst et al. 2019).

ExA-SPIM relies on tissue expansion and lower NA optics compared to microscopes that are typically used for high-resolution imaging. This approach has several advantages over imaging of cleared (non-expanded) tissues. First, optical engineering requirements are more forgiving for lenses with lower NA. As shown in (**Figure 1b**), lower NA lenses can have much higher etendues, fields of view, and much longer working distances. In other words, a large volumetric coverage (accessible resolvable voxels) is more feasible with lower NA lenses. In addition, these lenses are more easily corrected for common distortions, including field curvature, pincushion distortion, vignetting, and uniform resolution across the entire field of view (Yueqian & Herbert 2019). These lenses can be paired with large format CMOS sensors that offer voxel rates surpassing more commonly used scientific CMOS sensors. These technologies will continue to progress rapidly. For example, the recently announced 247 megapixel Sony IMX811 sensor[10] will be capable of delivering 12-bit images at up to 3 gigavoxels/sec.

Second, lower NA imaging is less sensitive to tissue-induced aberrations. Although clearing and expansion techniques render tissues transparent, remnant refractive index inhomogeneities still deteriorate image quality at

10. https://www.sony-semicon.com/en/products/is/industry/rolling-shutter.html

larger imaging depths (Weiss et al. 2021). This is more noticeable at higher NA, because the rays entering the objective at higher angles have longer path lengths through the tissue and are more susceptible to aberrations (**Figure S1**). For lower NA systems the differences in path lengths between the extreme and axial rays are smaller. For example, the effect of spherical aberration (e.g. loss of Strehl ratio, which may be a dominant aberration mode for imaging cleared and expanded tissues) increases with NA to the third power (Hecht 2015).

Third, the refractive index gradients in tissue are expected to decrease with the third power of the expansion factor (proportional to density) (Jacques 2013). As a consequence, tissue-induced aberrations reduce with the expansion factor to the third power. In contrast, the imaging path length through the tissue only increases with the expansion factor to the first power. These factors together may explain the advantage of expansion-assisted imaging (**Figure S1**). Further investigation into the optical properties of hydrogels and their constituents is necessary to fully support these hypotheses. ExA-SPIM still exhibits a decrease in image quality at larger imaging depths (**Figure 3 Supplementary Figure 1**). This can be reduced with dual-sided excitation (Dodt et al. 2007) as well as multi-view detection (Tomer et al. 2012).

One limitation of the current implementation of the ExA-SPIM is related to inefficient collection of signal photons. Given that signal collection scales approximately with NA^2, signal collection is 10× lower compared to a NA = 1.0 system ($(1/0.305)^2$). However, we find that the ExA-SPIM system can detect and resolve dim, nanoscale biological features with high signal-to-noise ratio (e.g., thin axons). Because of the large field of view, high SNR imaging requires 1000+ mW lasers. However, light intensities are similar to traditional SPIM systems because the power is distributed over a ~1 cm wide light sheet. Under these imaging conditions photobleaching is not detrimental (i.e., ~50% reduction in intensity after ~800 repeated exposures), suggesting that even higher laser intensities could be used for higher SNR imaging (**Figure S2**). To improve signal collection and enable even higher sensitivity ExA-SPIM imaging, a custom lens with NA = 0.5, FOV = 6.8, and a 35 mm working distance in liquid has been designed and is being fabricated. This new lens will enable ~50 - 150 nm effective lateral resolution in 3-12× expanded tissues, with 2.7× improved light collection efficiency.

Fundamentally, contrast, effective resolution and imaging speed in expansion microscopy are limited by the density of fluorescent molecules labeling the structure of interest and the photon budget. ExA-SPIM allows distributing the technical burden between optics and tissue expansion (**Figure S3**). In practice, a target resolution should first be specified, corresponding to a viable combination of NA and tissue expansion, taking into consideration light collection efficiency (NA dependent) and required working distance (expansion factor dependent).

Although we have focused on the combination of new microscopy with tissue expansion, the ExA-SPIM microscope design will be useful for many additional imaging applications. For example, the field of view of the ExA-SPIM is sufficient to image a cleared mouse brain without the need for tiling. Cleared mouse brain datasets with ~1.5 µm lateral resolution could be acquired at a speed of ~36 min/channel (**Figure S4**). In addition, the entire system could be converted to an inverted (Wu et al. 2013; Kumar et al. 2014) or open-top (McGorty et al. 2015; Glaser et al. 2017; Glaser et al. 2019; Barner et al. 2020; Glaser et al. 2022) architecture, which would enable large-scale imaging of tissue slabs with large aspect ratios that are up to 1 cm thick (**Figure 4 Supplementary Figure 1**). Similarly, an ExA-SPIM system with a lower resolution metrology lens could easily be built (see **Table S3**). These more mesoscale systems would provide extremely high imaging throughput (cm^3 per day) and could pave the way for new large-scale neuroanatomy investigations of human and non-human primate tissues.

Finally, new types of applications may also require multi-scale microscopy. For example, expansion microscopy could provide a super-resolution view of interactions between immune cells and solid tumors. This application may require 10× expansion, for better than 100 nm effective resolution, to distinguish immunofluorescence in immune cells and tumor cells, throughout millimeter-scale tissue samples (10 mm after expansion). Given that 10× expanded samples are mechanically fragile and difficult to handle and section, the large field of view and reduced need for physical sectioning of ExA-SPIM would be highly advantageous for these demanding imaging experiments.

In summary, our new ExA-SPIM approach represents a new substrate for innovation within the realm of large-scale fluorescence imaging. By leveraging technologies from the electronics metrology industry, in combination with whole-mount tissue expansion, the system provides: (1) nanoscale lateral resolution, (2) over large centimeter-scale volumes, (3) with minimal tiling and no sectioning, (4) high isotropy, and (5) fast imaging speed.

Materials and methods

Microscope design

A parts list and CAD model are available at https://github.com/AllenNeuralDynamics/exa-spim-hardware. A ZEMAX model is available at https://github.com/AllenNeuralDynamics/exa-spim-optics. The system has two main optical paths (**Figure S5**). The first excitation path shapes and delivers the light sheet to the specimen. Laser light is provided by a custom-made laser combiner containing a 200 mW 405 nm laser (LBX-405-180-CSB-OE, Oxxius), 1000 mW 488 nm laser (Genesis MX488-1000 STM OPS Laser-Diode System, Coherent Inc.), 1000 mW 561 nm laser (Genesis MX561-1000 STM OPS Laser-Diode System, Coherent Inc.), and 1000 mW 639 nm laser (Genesis MX639-1000 STM OPS Laser-Diode System, Coherent Inc.) (**Figure S6**). Due to the large light-sheet, the ExA-SPIM system benefits from high excitation lasers powers (1000+ mW), resulting in light intensities typically used in SPIM microscopy. Photobleaching is not detrimental at these imaging conditions. An acousto-optic tunable filter (AOTFnC-400.650-TN, AA Opto Electronic) controlled by a RF driver (MPDS8C-D65-22-74.158-RS, AA Opto Electronic) is used to modulate each laser and control the output power of the combiner. The output beam from the combiner is ~1.2 mm in diameter, which is expanded to 13.3 mm using two relay lenses with f = 3.6 mm (LMPLANFLN 50×, Olympus) and f = 40 mm (HLB M PLAN APO 5×, Shibuya Optical). The light path is then reflected vertically by a third kinematic mirror and focused along one axis by an achromatic cylindrical lens (ACY254-050-A-ML, Thorlabs). The cylindrical lens is mounted in a motorized rotation mount (C60-3060-CMR-MO, Applied Scientific Instrumentation). This enables precise electronic control over the rotation of the light sheet within the specimen. Control over this parameter is important, as the field of view (~10.6 mm) and depth of field of the detection lens (<10 μm) require the sheet to be rotated with <1 deg precision. The light from the cylindrical lens is focused onto an electrically tunable lens (EL-16-40-TCVIS-20D-C, Optotune AG). The actuating surface of the electrically tunable lens is conjugated to the back focal plane of the excitation objective (1-290419, Navitar) through two large 20 mm galvanometric scanning mirrors (QS20X-AG, Thorlabs), three additional kinematic mirrors, and a final relay consisting of a first lens with f = 200 mm (AC508-200-A-ML) and second lens with f = 300 mm (AC508-300-A-ML). The two galvanometric mirrors are not conjugated to the back focal plane of the excitation objective and are used in tandem to tilt and translate the light sheet to be co-planar with the detection lenses' focal plane. Similar to the cylindrical lens rotation, the light sheet must also be tilted to <1 deg precision across the ~8.0 mm vertical height of the imaging field of view.

The excitation objective has a focal length of f = 110 mm, NA = 0.133, and back aperture diameter of ~29.26 mm, with which the preceding excitation optics, results in a Gaussian excitation light sheet with NA ~0.1. The intensity profile across the width of the light sheet is also Gaussian, with a full-width half-maximum (FWHM) of ~12.5 mm. This corresponds to a reduced (60%) light intensity at the edges of the field of view. The lens is mounted in a custom dipping cap which extends the effective working distance from 39 mm in air to ~52 mm in water. The 1-mm thick window on the dipping cap was sealed with UV curing optical adhesive (NOA86, Norland Products). The lens is oriented vertically, such that the light sheet is delivered downward into the immersion chamber which is filled with an immersion medium.

Fluorescence is collected with a high etendue electronics metrology lens (VEO_JM DIAMOND 5.0×/F1.3, Vieworks Co., LTD; jointly developed and fabricated by Schneider-Kreuznach). Whereas the spherical aberration introduced in the excitation path is negligible, the same dipping cap design would result in severe spherical aberration on the detection path, where the aperture was larger (NA = 0.305). Imaging at these higher apertures necessitated imaging lenses designed for direct immersion into a liquid mounting medium. The VEO_JM DIAMOND detection lens is designed for co-axial illumination, involving a 35 mm thick BK7 glass (n = 1.52) beam splitter mounted on the front object side of the lens. The beam splitter couples white light into the lens for bright illumination of electronic components during inspection. This was leveraged for aberration-free imaging into a liquid mounting medium.

We removed the beam splitter and replaced it with an optically equivalent thickness of the aqueous mounting medium (30 - 35 mm for refractive indices between 1.33 - 1.56) and glass (4 mm total, including the chamber window and fluorescence filter). This scheme avoids the spherical aberrations that would otherwise plague imaging with an air-immersion lens into a non-air-based medium. The lens is positioned horizontally on the optical table outside of the immersion chamber. The lens images the specimen through a λ/10 50 mm diameter VIS-EXT coated fused silica window that is 3 mm thick (#13-344, Edmund Optics). The window was glued to the immersion chamber using UV curing optical adhesive (NOA86, Norland Products). A custom 44 mm diameter 1 mm

thick multi-bandpass fluorescence filter (ZET405/488/561/640mv2, Chroma) is inserted on the outer side of the immersion chamber and held in place with a retaining ring (SM45RR, Thorlabs). Placing the filter on the object side of the lens results in a cone angle of incidence of 17.8 deg. This results in a spectral shift and broadening of transmitted light, which was modeled to account for adequate suppression of scattered light at the excitation laser wavelengths.

The lens is attached to the camera (VP-151MX-M6H00, Vieworks Co., LTD) using a custom mechanical assembly that enables tipping and tilting of the lens and camera relative to the immersion chamber window. To reduce fixed pattern noise at low light levels, we requested that the manufacturer permanantly disable the photo response non-uniformity (PRNU) correction mode. The camera uses the Sony IMX411 sensor, which features a 14192×10640 array of 3.76 µm pixels. The 5.0× magnification of the detection lens implies sampling at 0.75 µm in the specimen plane. Because the detection lens is not infinity-corrected, it is not possible to change tube lenses to change the pixel sampling. Therefore although the optical resolution of the detection lens is ~1.0 µ()m, the sampling limited resolution based on the Nyquist criterion is 1.5µm. However, it is worth noting that Vieworks Co. produces cameras with pixel-shifting technology[11], which would enable finer sampling if needed. The cooling fan on the camera was replaced with a quieter fan operating at 2400 rpm (Noctua NF-A6x25 FLX, Premium Quiet Fan, 3-Pin, 60 mm, Noctua). Using an alignment laser, the entire assembly was aligned to the window. The entire assembly is also mounted on a rail system (XT95, Thorlabs) that enables precise axial alignment of the assembly relative to the chamber window.

The sensor can be operated with 12, 14, or 16-bit analog to digital (A/D) conversion, each of which provides a trade-off between noise and data throughput. When operated with 14-bit A/D, the line time of the sensor is 20.15 µs. With 14192 pixels per row on the sensor, this corresponds to an imaging speed of 703×10^6 voxels/sec. The line times and imaging speeds at 12 and 16-bit are 15.00 and 45.44 µs respectively, corresponding to 946 and 312×10^6 voxels/sec. This contrasts with a state-of-the-art sCMOS sensor with 2048 pixels per row, where even at the fastest 4.89 µs line time, the imaging speed is only 418×10^6 voxels/sec. In other words, the Sony IMX411 sensor provides more pixel parallelization within each row. This enabled twice the voxel rate with four times the pixel dwell time. See **Note S1** for further discussion on comparing the speed and sensitivity of cameras.

The specimens, in this case an expanded gels, were mounted in a customized holder, which was attached to a motorized XY stage (MS-8000, Applied Scientific Instrumentation) and Z stage (LS-100, Applied Scientific Instrumentation), for scanning and tiling based image acquisition.

Microscope control

The microscope was controlled using a high-end desktop workstation (SX8000, Colfax Intl). The workstation was equipped with a motherboard with five PCIe 4.0x16 and one PCIe 4.0x8 slots (X12DAI-N6, Supermicro), most of which are required for the various electronics needed to control the ExA-SPIM. One slot was used for the frame grabber (Coaxlink Octo, Euresys), which streams imaging data from the camera onto a fast local 12.8 TB NVME drive (7450 Max 12800GB 3 DWPD Gen4 15mm U.3, Micron). A second slot was used for the data acquisition (DAQ) card (PCIe-6738, National Instruments) used for generating the various digital and analog voltage signals. A third slot was used for the high-speed network interface card (ConnectX-5 EN MCX515A-CCAT QSFP28 Single Port 100GbE, Mellanox) to transfer data off the local NVME drive, over the network, and onto a networked server. A fourth slot was occupied by the workstation GPU (A4000, NVIDIA). The workstation was also connected to a controller (TG-16, Applied Scientific Instrumentation) via a USB connection. The TG-16 controller was equipped with cards for controlling the motorized X, Y, and Z stages, the electrically tunable lens, and the cylindrical lens rotation mount. Finally, each laser within the combiner was connected to the computer via a USB connection, as well as the RF driver of the AOTF. The DAQ acted as the master controller of the entire system. Analog output voltages were used to drive or trigger the electrically tunable lens, two scanning galvanometric mirrors, camera, scanning stage, and the RF outputs to the AOTF for each laser.

Acquisition software

The microscope was controlled using custom software written in Python https://github.com/AllenNeuralDynamics/exaspim-control and was operated on the Windows 10 operating system. The software could control and configure

11. See the pixel-shifting section at: https://vision.vieworks.com/en/technology

all of the electronically controlled hardware devices and uses Napari[12] as the graphical user interface (GUI) for image streaming and visualization. An imaging experiment consisted of a series of nested loops, which included looping over the total number of frames within a given tile, looping over the total number of channels within a tile, and finally tiling in two dimensions to cover the entire tissue volume. A multiprocessing, double buffering scheme was used to capture a tile while the previous tile was being transferred over the network to longer term storage. All hardware was controlled using a custom library for developed for generalized microscope control https://github.com/AllenNeuralDynamics/voxel.

To achieve robust and reliable acquisition at the speed required by the ExA-SPIM, we used two data streaming strategies. The first used the open-source eGrabber frame grabber Python API[13] and open-source Acquire package (https://github.com/acquire-project) (Clack et al. 2023), specifically the Python API Acquire-Zarr (Liddell et al. 2025). Acquire is a new state-of-the-art microscope acquisition project which enables the ExA-SPIM system to stream data at the required rate, directly to OME-Zarr file format (V2 or V3), with either ZStandard or LZ4 compression, a variable chunk size, a variable shard size (for V3), and an optional multi-resolution pyramid, all of which help streamline downstream data storage and handling. The second strategy used the ImarisWriter library (Beati et al. 2020). This option enabled high-speed data streaming with online lossless compression (LZ4 with bit shuffling) and real-time writing of a multi-resolution pyramid.

On average, the lossless compression ratio using either ImarisWriter or Acquire was ~1.5-4× depending on the bit mode of the camera (e.g. 12, 14, or 16 bits) . This reduced the overall effective data rate of the system and eased network transfers of the data to centralized storage. A schematic of the acquisition pipeline is shown in **Figure S7**.

Point spread function quantification

To quantify the point spread function of the ExA-SPIM microscope we imaged fluorescent 0.2 µm TetraSpeck™ microspheres (Invitrogen, cat no. T7280, lot no. 2427083) using 561 nm excitation. A cube of expanding hydrogel containing a 10% (v/v) microbead solution was prepared 40 µL of microspheres solution was added to 360 µL of activated Stock X monomer solution, as described in (Asano et al. 2018). The solution was briefly vortexed, and carefully pipetted into an array of 2 mm^3 wells in a silicone mold. The mold was placed in a sealed petri dish containing damp Kimwipes® to maintain humidity and incubated at 37°C for 2 hours. After incubation, the polymerized bead phantoms were placed into 0.05× SSC buffer for at least 24 hrs to expand and equilibrate prior to imaging. After volumetric imaging, the resulting imaging stack was analyzed using custom written Python code https://github.com/AllenNeuralDynamics/exa-spim-characterization. The results shown in **Figure 2** are averaged from >10,000 individual beads.

Field curvature quantification

We used the field curvature quantification methods developed for the Benchtop mesoSPIM (Vladimirov et al. 2024). Briefly, the field curvature was measured using a high-precision Ronchi ruling with 120 lines per mm (62-201, Edmund Optics). The ruling was mounted into the system, and aligned to be normal (i.e., flat) with respect to the imaging path. The ruling was trans-illuminated using light-emitting diodes (LEDs) at 450 nm (M450LP2, Thorlabs), 530 nm (M530L4, Thorlabs), 595 nm (M595L4, Thorlabs), and 660 nm (M660L4, Thorlabs). To provide uniform illumination, the LEDs were collimated to a diameter of ~20 mm and passed through a diffuser (ED1-C20, Thorlabs). Image stacks were captured by scanning the Ronchi ruling in 1 µm steps through the imaging path focal plane (2 mm total scan range) with illumination at either 450 nm, 530 nm, 595 nm, or 660 nm. The resulting image stack was split into a 16×16 grid of regions of interest (ROI), each 887× 665×2000 pixels. Within each ROI, the contrast of each frame in the stack was calculated using the 5th and 95th percentiles of intensity within the frame, where the contrast, $C = (I_{max} - I_{min})/(I_{max} + I_{min})$. The resulting contrast versus depth curve was fit to a normal distribution to extract the depth (i.e., index) corresponding to maximum contrast. The indices were radially averaged across the 16×16 grid of ROIs, yielding an estimate of the imaging lens field curvature within each of the four tested wavebands. Custom Python scripts were used to run the analysis https://github.com/AllenNeuralDynamics/exa-spim-characterization.

12. https://napari.org
13. https://www.euresys.com

Lens distortion quantification

The lens distortion was measured using a target (62-950, Edmund Optics) with 125 µm diameter dots spaced every 250 µm in a grid pattern. The target was mounted and trans-illuminated using LEDs in the same manner as the field curvature quantification. A single image was acquired with the target at the focal plane of the imaging lens. The resulting image was quantified by first segmenting and calculating the centroid of each dot. The calculated position of each dot was then compared to the theoretical dot position. The percent distortion for each dot was defined as the difference between the experimental and theoretical positions, normalized by the theoretical position. The resulting distortion values were radially averaged, yielding the lens distortion as a function of position from the center of the lens field of view. Custom Python scripts were used to run the analysis https://github.com/AllenNeuralDynamics/exa-spim-characterization.

Camera sensitivity comparison

A bead phantom (see point spread function measurement) was used to compare the sensitivity of the large-format CMOS camera and a scientific CMOS camera (Orca Flash V3, Hamamatsu). A single bead was first imaged with the scientific CMOS camera, varying the effective pixel rate or imaging speed. The scientific CMOS camera was then removed from the microscope and replaced with the large-format CMOS camera. The same bead was located and imaged again at various effective pixel rates. The bead was located in all image stacks, and the signal-to-noise ratio of the bead was quantified as the signal of the bead, minus the average background signal, divided by the background noise. A custom written Python code was used to run the analysis https://github.com/AllenNeuralDynamics/exa-spim-characterization. It is worth noting that the Orca Flash V3 is an older scientific CMOS camera. Newer cameras, such as the Orca BT Fusion with improved noise characteristics (1.0 e- versus 1.6 e- read noise and 95% versus 85% peak quantum efficiency) are now available. However, these differences would not significantly change the results shown in **Figure 2e**. **Note S1** contains a deeper discussion on comparing the speed and sensitivity of cameras.

Local data storage and handling

Data was streamed using the Acquire or ImarisWriter onto a local NVME drive in the acquisition workstation. Upon the completion of a tile, the resulting files were transferred over the high-speed network using xcopy[14] onto a 670 TB enterprise storage server from VAST data. This occurred in parallel with the acquisition of the next imaging tile. Upon completion of the transfer, the tile was deleted off the acquisition workstation's NVME drive.

Image compression and cloud transfer

The raw data for each color channel consisted of a set of overlapping 3D image tiles. For the ImarisWriter acquisition workflow, the images were stored in Imaris IMS file format[15], an HDF5-based format which enables fast parallel writing to local storage. However, this format is not well suited to being archived in cloud (object) storage since accessing an arbitrary data chunk requires seeking a file. Thus, the data was converted to OME-Zarr format, which supports parallel read-write over the network and has a rich metadata structure (Moore et al. 2021; Moore et al. 2023). OME-Zarr is also integrated with visualization and annotation tools used for downstream visualization and analysis, including Horta Cloud (https://github.com/JaneliaSciComp/hortacloud) and Neuroglancer (https://github.com/google/neuroglancer) (Maitin-Shepard et al. 2021). With up to four channels, the storage footprint for a single dataset can reach hundreds of terabytes. Therefore, the storage ratios and compression/decompression speeds of various lossless codecs were compared. Blosc ZStandard yielded the highest storage ratios, with compression speeds comparable to LZ4 at lower 'clevel' settings (e.g., 1-3). Dask[16] was used to parallelize the compression and OME-Zarr writing over a high-performance computing (HPC) cluster consisting of 16 nodes, each with 32 Intel CPUs with Advanced Vector Instructions 2 (AVX2) and 256 GB RAM. Image chunks were read in parallel from high-bandwidth network storage, compressed in memory, and written directly to AWS S3 and Google Cloud Storage buckets. Combined throughput (chunk read, compress, write) reached over 2 GB/s, with execution time dominated by read-write I/O operations. The image compression and

14. https://learn.microsoft.com/en-us/windows-server/administration/windows-commands/xcopy
15. https://imaris.oxinst.com/support/imaris-file-format
16. https://www.dask.org

cloud transfer code is available at https://github.com/AllenNeuralDynamics/aind-data-transfer. For the Acquire acquisition workflow, datasets were streamed directly to the OME-Zarr format.

Image stitching

ExA-SPIM image stitching used a combination of on-premises and cloud-based resources. Datasets were first converted from OME-Zarr to N5 and stitched using BigStitcher on the Google Cloud Platform (GCP) (Hörl et al. 2019). Tile placement transformations were based on interest points. The interest point based tile registration consisted of three steps: identification of interest points, finding corresponding interest points between tiles, and optimizing for tile transformation parameters with respect to the distance of corresponding interest points. We first performed a translation only stitching routine, followed by a full affine transformation optimization. The affine transformation was regularized by a rigid transformation and corner tiles were kept fixed to prevent the global scaling of the sample and divergent solutions at the corner tiles. As a rule of thumb, several thousand interest points per overlapping region were required for a reliable identification of correspondences and successful optimization. Once the alignment transformations were calculated, the tiles were fused using the on-premises HPC into a single contiguous volume in the N5 format. A representative dataset (~100 TB in raw uncompressed size) can be fused in ~24 hours using 16 nodes (32 cores each, 480 total), with 16 GB of RAM per core (7.68 TB total) and an output chunk size of 256, 256, 256 pixels. 2 cores per node are reserved as overhead per spark worker (i.e., 32 total for 16 nodes). Fused datasets along with the raw tiled datasets and the tile placement transformations are deposited in an Amazon Web Services S3 aind-open-data data bucket. The N5 datasets were converted to OME-Zarr for visualization with Neuroglancer, or KTX[17] for visualization with HortaCloud. The current pipeline involves several file format conversion steps and transfers between on-premises and cloud-based platforms. Future pipelines will standardize around OME-Zarr and be completely operable in the cloud. Only the initial data conversion and compression step would be computed on-premises.

Image visualization and annotation

To generate whole-brain single neuron reconstructions we use HortaCloud, an open-source streaming 3D annotation platform enabling fast visualization and collaborative proofreading of terabyte-scale image volumes. Human annotators proofread stitched image volumes using HortaCloud in a web browser on a personal workstation. Starting from the soma, the axonal and dendritic arbors were traced through all terminals by laying down connected points along the neurite, producing a piecewise-linear approximation of neuronal trees (Economo et al. 2016).

Whole mouse brain tissue processing

Briefly, the samples were cleared, immunolabeled and expanded as described below. Detailed protocols for preparing cleared and expanded brains are available at [(Ouellette et al. 2023), dx.doi.org/10.17504/protocols.io.n92ldpwjxl5b/v1].

Viral labeling in mice

Adult transgenic Cre driver mice between ages p21 to p35 received systemic injections, via the retro-orbital sinus, of a 100 µL mixture of Cre-dependent Tet transactivator (AAV-PHP-eB_Syn-FlexTRE-2tTA, typical dose 6.0×10^{8} gc/mL) and a reporter virus (AAV-PHP-eB_7x-TRE-tdTomato, typical dose 1.8×10^{11} gc/mL) (Addgene plasmid id: #191210 and, #191207). Viral vector-mediated recombination was achieved by retro-orbital injection of AiP1999 - pAAV-AiE2255m-minBG-iCre(R297T)-BGHpA (Addgene id: 223843) along with the two aforementioned vectors. The viral titers of the tTA virus used were empirically adjusted based on the Cre driver line to yield sparsely labeled brains. Viruses were obtained from either the Allen Institute for Brain Sciences viral vector core, the University of North Carolina, BICCN-Neurotools core and were prepared in an AAV buffer consisting of 1× PBS, 5% sorbitol, and 350mM NaCl.

Collection

All experimental procedures related to the use of mice were approved by the Institutional Animal Care and Use Committee of the Allen Institute for Brain Science, in accordance with National Institutes of Health (NIH)

17. https://registry.khronos.org/KTX

guidelines. Four weeks after viral transfection, mice (~p70) were anesthetized with an overdose of isoflurane and then transcardially perfused with 10 mL 0.9% saline at a flow rate of 9 mL/min followed by 50 mL 4% paraformaldehyde in PBS at a flow rate of 9 mL/min. Brains were extracted and post-fixed in 4% paraformaldehyde at room temperature for 3-6 hours and then left at 4°C overnight (12-14 hours). The following day, brains were washed in 1× PBS to remove all traces of excess fixative.

Delipidation

Whole brain delipidation was performed in two stages. First, brains were dehydrated through a gradient of tetrahydrofuran (THF) in deionized water at 4°C and then delipidated in anhydrous dichloromethane (DCM) at 4°C. The brains were rehydrated into water through a gradient of THF and then placed in 1× PBS. Second, whole brains were transferred from 1× PBS to a biphasic buffer (SBiP) for 5 days at room temperature and then rinsed in a detergent buffer (B1n) for 2 days.

Immunolabeling

Delipidated brains were equilibrated in a detergent buffer (PTxw) and then incubated in PTxw containing the primary antibody (10 µg/brain) at room temperature for 11 days. After thorough washing in PTxw, a solution of the secondary antibody (20 µg/brain) was added for 11 days at room temperature. Brains were then rinsed thoroughly with PTxw and transferred to 1× PBS.

Gelation and expansion

Immunolabeled brains were equilibrated in MES buffered saline (MBS) followed by incubation in acryloyl-X SE (AcX) at 4°C on wet ice for 4 days . The AcX solution was then rinsed off with 1× PBS and the brain was then transferred to a solution of StockX activated with VA-044 at 4°C on wet ice for 4 days. After StockX incubation, whole brains were placed in a polymerization chamber and filled with activated StockX solution. The chamber was sealed with a coverslip, placed in an inert atmosphere of N_2, and baked at 37°C for 4+ hours until hydrogel formation. The hydrogel was then digested with proteinase K for 10+ days, until the tissue cleared. Upon completion of digestion, the brain was rinsed with 1× PBS and expanded in 0.05× saline sodium citrate (SSC) until 3× expansion was achieved.

Macaque brain tissue processing

The process for preparing the macaque brain samples is described below.

Spinal injection procedure and motor cortex collection

To retrogradely label corticospinal neurons in the hand-wrist and trunk regions of primary motor cortex in a pigtail macaque, we injected a retro AAV vector (rAAV2-CAG-tdTomato; Addgene plasmid #59462 packaged in-house, titer of 1.88×10^{13}) into the left lateral funiculus and ventrolateral part of the gray matter in the C6/C7 spinal segments. All animal procedures have been approved by the University of Washington IACUC committee and conformed to the NIH's Guide for the Care and Use of Laboratory Animals.

An 11 year and 4 months old female *Macaca nemestrina* (10.55 kg) designated for the tissue distribution program was anaesthetized with isoflurane after an initial sedation with ketamine. The monkey was paralyzed with a neuromuscular blocker and artificially ventilated. The animal was monitored by a trained surgical technician for pulse oximetry, body temperature, ECG, blood pressure, capnography, and inspired oxygen. External thermal support was provided for the duration of the surgery, and an intravenous line for i.v. drug and isotonic fluid administration, a urethral catheter was inserted to maintain fluid volume and physiological homeostasis. Under aseptic conditions, a partial laminectomy of the C5-C7 vertebrae was performed to expose the left dorsal surface of the cervical enlargement.

Using a stereotaxic manipulator (Kopf Instruments, Tujunga, CA) on a custom frame, targeted microinjections were performed with a Nanoject II (Drummond Scientific, Broomall, PA). A glass pipette with a broken tip (barrel of tip = 50 ×m), filled with rAAV2-CAG-tdTomato , was inserted into the spinal cord through small longitudinal incision of the dura. Using the dorsal root entry points as a guide, 7 injection tracts spanning dorsal-ventral were used to target the lateral funiculus and ventrolateral part of the gray matter in the C6/C7 spinal segments. Each

tract had five injections (138 nL of virus at 23 nL/second) positioned 100 μm apart spanning -4.1 to -3.7 mm from the surface of the cord. The seven tract locations spanned 2.2 mm anterior-posterior and were in two rows (1 mm apart), evenly spread with slight adjustments to avoid hitting the vasculature. A one-minute wait period was used prior to each first injection within the tract, a two-minute wait period after each injection before moving the pipette and a five-minute wait period before removing the electrode after the final injection for each tract. The injector's efficacy at ejecting virus was confirmed between each injection tract.

After the injections were complete, artificial dura was placed over the durotomy, the musculature and skin were sutured, and an anti-paralytic agent (atropine) was delivered. Post-operative monitoring and care were performed to minimize pain and distress. Thirty days after the original injections, the animal was anaesthetized as described above, and then euthanized using a lethal dose of pentobarbital solution. After death, the animal was perfused transcardially with sodium-free oxygenated ice-cold artificial cerebrospinal fluid (NMDG-aCSF in mM): 92 NMDG, 25 glucose, 30 $NaHCO_3$, 20 HEPES, 10 $MgSO_4$, 2.5 KCl, 1.2 NaH_2PO_4, 0.5 $CaCl_2$, 3 sodium pyruvate, 2 thiourea, 5 sodium ascorbate. After perfusion, the brain was removed and the right hemisphere trunk and hand wrist subregions of primary motor cortex were dissected and stored in NMDG-saline on ice. A portion (2 cm^3) of the motor cortex was further sub-dissected and stored in freshly made 4% paraformaldehyde in 0.1 M phosphate-buffered saline for later processing.

Delipidation, immunolabeling, gelation, and expansion

Macaque tissue was processed in the same manner as whole mouse brains.

Human brain tissue collection, delipidation, labeling, gelation, and expansion

Deidentified postmortem adult human brain tissue (61 year old male, Hispanic, no known history of neuropsychiatric or neurological conditions) was obtained with permission from next-of-kin by the San Diego Medical Examiner's Office. Tissue procurement was reviewed by the Western Institutional Review Board (WIRB) and did not constitute human subject research requiring Institutional Review Board (IRB) review, in accordance with federal regulation 45 CFR 46 and associated guidance. Postmortem tissue collection was performed in accordance with the Uniform Anatomical Gift Act described in Health and Safety Code §§ 7150, et seq., and other applicable state and federal laws and regulations.

Tissue was manually sliced into 1 cm coronal slabs, flash frozen with liquid nitrogen, vacuum sealed and stored at −80°C by the Allen Institute Tissue Processing Team. One slab from the occipital pole was drop-fixed in 4% PFA for approximately 12 hours at 4°C, and tissue regions containing visual cortex were dissected into ~1 cm blocks for histological processing. Individual blocks were then SHIELD-fixed (Lifecanvas Technologies) prior to sectioning at 100 μm on a sliding freezing microtome to further protect protein antigenicity and tissue architecture. Individual free-floating sections were then passively delipidated (LifeCanvas Technologies) for one week prior to immunolabeling. Delipidated sections were subsequently immunolabeled for SMI-32, which identifies heavy chain neurofilaments that make up axon scaffolds in long-range projection neurons. Free-floating sections were blocked in NGSTU (5% goat serum, 0.6% Triton X-100, 4M urea in 1× PBS) overnight, incubated with a primary antibody (rabbit anti-neurofilament 200, Sigma Aldrich N4142) diluted 1:500 in NGSTU + 0.02% sodium azide for 5 days, followed by a secondary antibody incubation (goat anti-rabbit AF488, ThermoFisher A-11034) diluted 1:100 in NGST (5% goat serum, 0.6% Triton X-100 in 1× PBS) for 4 days. Due to the thinness (100 um) of this tissue compared to an entire mouse brain, the gelling protocol used varied slightly from the whole brain gelling protocol described above. Most notably, the thermal initiator used was ammonium persulfate (APS) instead of VA-044, the tissue was polymerized at room temperature for 3 days, and the resulting tissue-hydrogel matrix was digested using a 1:50 concentration of proteinase-k in buffer (5% Sodium Dodecyl Sulfate, 5% Triton X-100, 10% 1M TRIS pH8).

Sample mounting

The expanded samples were trimmed to produce smooth edges and then were placed in a custom-built anodized imaging chamber. The sample chamber assembly was performed in a large bath of the expansion and imaging solution (0.05× SSC). The smooth edges of the hydrogel were placed against the chamber panels corresponding to the excitation and emission path and then the chamber removed from the bath. A warm (55°C) solution of 2% agarose, in the same 0.05× SSC as used during expansion, was carefully poured into the chamber space behind

the hydrogel for structural rigidity during imaging and let cool to room temperature until solid. The chamber was then sealed and placed in 0.05× SSC for equilibration overnight before imaging. The detailed protocol for mounting the expanded hydrogels is available on protocols.io: [(Ouellette et al. 2023), https://www.protocols.io/view/whole-mouse-brain-delipidation-immunolabeling-and-cmqbu5sn?step=12].

Data availability statement

Imaging datasets for this paper are available at:

```
s3://aind-open-data/exaSPIM_708373_2024-04-02_19-49-38
s3://aind-open-data/exaSPIM_671477_2024-01-08_17-03-04
s3://aind-open-data/exaSPIM_Z13288-QN22-26-036_2023-03-26_09-27-21
s3://aind-open-data/exaSPIM_H17.24.006-CX55-31B_2023-05-11_14-59-09
```

Instructions for how the data is organized and how it can be accessed is available at: https://allenneuraldynamics.github.io/data.html.

Code availability statement

Code is available as listed below. Please see the methods sections for additional usage details.
Microscope control: https://github.com/AllenNeuralDynamics/exaspim-control
Acquire video streaming: https://github.com/acquire-project
Hardware files: https://github.com/AllenNeuralDynamics/exa-spim-hardware
Optical files: https://github.com/AllenNeuralDynamics/exa-spim-optics
Characterization scripts: https://github.com/AllenNeuralDynamics/exa-spim-characterization
Compression and cloud transfer: https://github.com/AllenNeuralDynamics/aind-data-transfer

Acknowledgements

We thank the project management team at the Allen Institute for Neural Dynamics for helping to coordinate this work; the CZI Imaging Science team for support and collaborative work on the Acquire software project; Stephan Preibisch, Tobias Pietzsch, and the Janelia Open Science Software Initiative (https://www.janelia.org/open-science/overview/open-science-software-initiative-ossi) for support with BigStitcher; Nikita Vladimirov for the field curvature quantification methods; Jon Daniels from Applied Scientific Instrumentation for help and support with ASI related hardware; Keith Russell at Vieworks and Eric Jansenn from Euresys for help with the VP-151MX camera; Peter Majer and Sacha Guyer from Bitplane for assistance with the ImarisWriter API; Magnus Greger, Stuart Singer, Jim Sullivan from Schneider-Kreuznach and Joe Corsi from Navitar for assistance with the metrology lenses; and Tim Wang and Boaz Mohar for feedback on the manuscript. In addition, we thank the Allen Institute Animal Care, Transgenic Colony Management, and Lab Animal Services for mouse husbandry, injections, perfusions; the Allen Institute Tissue Processing Team; the Washington National Primate Research Center veterinary and technical staff; the San Diego Medical Examiner's Office. Supported by the Paul G. Allen Foundation and NIH R00CA240681 (AG), RF1MH128841 (KS and JC), U19NS123714 (KS and JC), R01NS123959 (ND and BK), U19NS137920 (partial support for JB), U42OD011123, and P51OD010425 for supporting this work.

Ethics declarations

A.G., J.C., and K.S. have filed for a patent on aspects of the ExA-SPIM system.

Author contributions

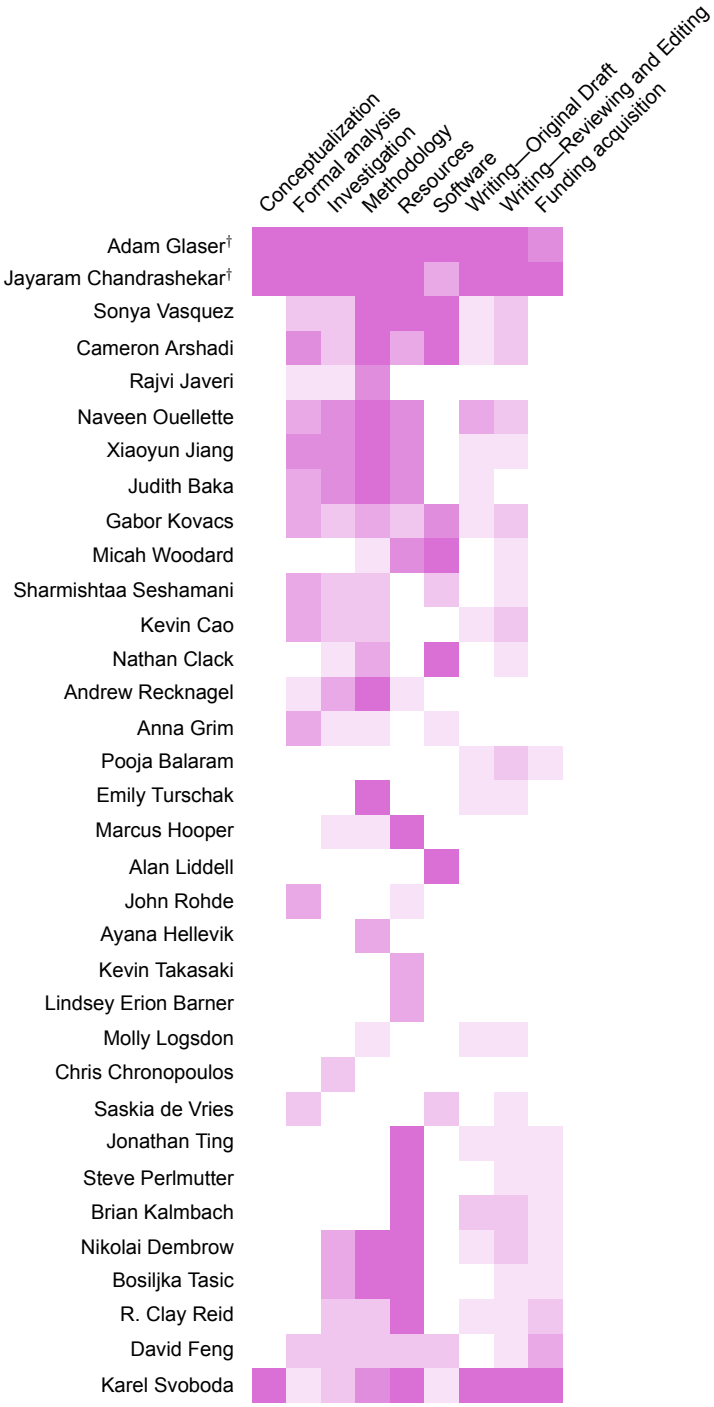

J.T. devised and validated the attenuated iCre mutant (R297T) for improved fidelity of recombination in the context of cell type specific enhancer AAV vectors.

References

Asano, S. M., R. Gao, A. T. Wassie, P. W. Tillberg, F. Chen, & E. S. Boyden. 2018. "Expansion Microscopy: Protocols for Imaging Proteins and RNA in Cells and Tissues." *Current Protocols in Cell Biology* 80: e56.

AU - Chi, J., A. AU - Crane, Z. AU - Wu, & P. AU - Cohen. 2018. "Adipo-Clear: A Tissue Clearing Method for Three-Dimensional Imaging of Adipose Tissue." *JoVE,* e58271.

Barner, L. A., A. K. Glaser, H. Huang, L. D. True, & J. T. Liu. 2020. "Multi-resolution open-top light-sheet microscopy to enable efficient 3D pathology workflows" [in en]. *Biomedical Optics Express* 11: 6605.

Beati, I., E. Andreica, & P. Majer. 2020. "ImarisWriter: Open Source Software for Storage of Large Images in Blockwise Multi-Resolution Format." *arXiv.*

Becker, K., N. Jährling, S. Saghafi, R. Weiler, & H. U. Dodt. 2012. "Chemical Clearing and Dehydration of GFP Expressing Mouse Brains" [in eng]. *PLoS One* 7: e33916.

Chakraborty, T., M. K. Driscoll, E. Jeffery, M. M. Murphy, P. Roudot, B.-J. Chang, S. Vora, et al. 2019. "Light-sheet microscopy of cleared tissues with isotropic, subcellular resolution" [in En]. *Nature Methods* 16: 1109–1113.

Chang, J.-B., F. Chen, Y.-G. Yoon, E. E. Jung, H. Babcock, J. S. Kang, S. Asano, et al. 2017. "Iterative expansion microscopy." *Nature Methods* 14: 593–599.

Chen, D., F. Segovia-Miranda, N. Walker, J. I. Valenzuela, M. Zerial, & E. W. Myers. 2020. "Bridging scales in scattering tissues via multifocal two-photon microscopy." *bioRxiv,* 2020.06.11.146704.

Chen, F., P. W. Tillberg, & E. S. Boyden. 2015. "Optical imaging. Expansion microscopy" [in eng]. *Science* 347: 543–8.

Chen, F., A. T. Wassie, A. J. Cote, A. Sinha, S. Alon, S. Asano, E. R. Daugharthy, et al. 2016. "Nanoscale imaging of RNA with expansion microscopy" [in en]. *Nature Methods* 13: 679–684.

Chen, R., X. Cheng, Y. Zhang, X. Yang, Y. Wang, X. Liu, & S. Zeng. 2021. "Expansion tomography for large volume tissue imaging with nanoscale resolution." *Biomed. Opt. Express* 12: 5614–5628.

Chen, S., & K. Svoboda. 2020. "'Uniclear' water-based brain clearing for light sheet imaging of electrode tracks." *protocols.io.*

Chen, Y., X. Li, D. Zhang, C. Wang, R. Feng, X. Li, Y. Wen, et al. 2020. "A Versatile Tiling Light Sheet Microscope for Imaging of Cleared Tissues." *Cell Reports* 33.

Cheng, Y., N. Grigorieff, P. A. Penczek, & T. Walz. 2015. "A Primer to Single-Particle Cryo-Electron Microscopy." *Cell* 161: 438–449.

Cho, I., & J.-B. Chang. 2022. "Simultaneous expansion microscopy imaging of proteins and mRNAs via dual-ExM." *Scientific Reports* 12: 3360.

Chozinski, T. J., A. R. Halpern, H. Okawa, H. J. Kim, G. J. Tremel, R. O. Wong, & J. C. Vaughan. 2016. "Expansion microscopy with conventional antibodies and fluorescent proteins" [in eng]. *Nature Methods* 13: 485–8.

Chung, K., & K. Deisseroth. 2013. "CLARITY for mapping the nervous system" [in eng]. *Nat Methods* 10: 508–13.

Clack, N., A. Liddell, & A. Sweet. 2023. "Acquire: a multi-camera video streaming software focusing on microscopy." *Zenodo.*

Costantini, I., J. P. Ghobril, A. P. Di Giovanna, A. L. Allegra Mascaro, L. Silvestri, M. C. Mullenbroich, L. Onofri, et al. 2015. "A versatile clearing agent for multi-modal brain imaging" [in eng]. *Scientific Reports* 5: 9808.

Daetwyler, S., & R. P. Fiolka. 2023. "Light-sheets and smart microscopy, an exciting future is dawning." *Communications Biology* 6: 502.

Damstra, H. G., B. Mohar, M. Eddison, A. Akhmanova, L. C. Kapitein, & P. W. Tillberg. 2022. "Visualizing cellular and tissue ultrastructure using Ten-fold Robust Expansion Microscopy (TREx)." Edited by M. Lakadamyali, S. R. Pfeffer, & X. Shi. *eLife* 11: e73775.

Dean, K., P. Roudot, E. Welf, G. Danuser, & R. Fiolka. 2015. "Deconvolution-free Subcellular Imaging with Axially Swept Light Sheet Microscopy" [in eng]. *Biophys J* 108: 2807–15.

Dodt, H.-U., U. Leischner, A. Schierloh, N. Jährling, C. P. Mauch, K. Deininger, J. M. Deussing, et al. 2007. "Ultramicroscopy: three-dimensional visualization of neuronal networks in the whole mouse brain" [in English]. *Nat Methods* 4: 331–336.

Economo, M. N., N. G. Clack, L. D. Lavis, C. R. Gerfen, K. Svoboda, E. W. Myers, & J. Chandrashekar. 2016. "A platform for brain-wide imaging and reconstruction of individual neurons." *eLife* 5: e10566.

Ertürk, A., K. Becker, N. Jährling, C. P. Mauch, C. D. Hojer, J. G. Egen, F. Hellal, et al. 2012. "Three-dimensional imaging of solvent-cleared organs using 3DISCO" [in en]. *Nature Protocols* 7: 1983–1995.

Fan, J., J. Suo, J. Wu, H. Xie, Y. Shen, F. Chen, G. Wang, et al. 2019. "Video-rate imaging of biological dynamics at centimetre scale and micrometre resolution." *Nature Photonics* 13: 809–816.

Fernandez-Leiro, R., & S. H. W. Scheres. 2016. "Unravelling biological macromolecules with cryo-electron microscopy." *Nature* 537: 339–346.

Gao, G., D. Miyasato, L. A. Barner, R. Serafin, K. W. Bishop, W. Xie, A. K. Glaser, et al. 2023. "Comprehensive Surface Histology of Fresh Resection Margins With Rapid Open-Top Light-Sheet (OTLS) Microscopy." *IEEE Transactions on Biomedical Engineering* 70: 2160–2171.

Gao, R., S. M. Asano, S. Upadhyayula, I. Pisarev, D. E. Milkie, T.-L. Liu, V. Singh, et al. 2019. "Cortical column and whole-brain imaging with molecular contrast and nanoscale resolution." *Science* 363: eaau8302.

Glaser, A. K., K. W. Bishop, L. A. Barner, E. A. Susaki, S. I. Kubota, G. Gao, R. B. Serafin, et al. 2022. "A hybrid open-top light-sheet microscope for versatile multi-scale imaging of cleared tissues." *Nature Methods* 19: 613–619.

Glaser, A. K., N. P. Reder, Y. Chen, E. F. McCarty, C. Yin, L. Wei, Y. Wang, L. D. True, & J. T. Liu. 2017. "Light-sheet microscopy for slide-free non-destructive pathology of large clinical specimens" [in en]. *Nature Biomedical Engineering* 1: 0084.

Glaser, A. K., N. P. Reder, Y. Chen, C. Yin, L. Wei, S. Kang, L. A. Barner, et al. 2019. "Multi-immersion open-top light-sheet microscope for high-throughput imaging of cleared tissues" [in En]. *Nature Communications* 10: 1–8.

Gong, H., D. Xu, J. Yuan, X. Li, C. Guo, J. Peng, Y. Li, et al. 2016. "High-throughput dual-colour precision imaging for brain-wide connectome with cytoarchitectonic landmarks at the cellular level." *Nature Communications* 7: 12142.

Gong, H., S. Zeng, C. Yan, X. Lv, Z. Yang, T. Xu, Z. Feng, et al. 2013. "Continuously tracing brain-wide long-distance axonal projections in mice at a one-micron voxel resolution." *NeuroImage* 74: 87–98.

Guo, M., Y. Li, Y. Su, T. Lambert, D. D. Nogare, M. W. Moyle, L. H. Duncan, et al. 2020. "Rapid image deconvolution and multiview fusion for optical microscopy." *Nature Biotechnology* 38: 1337–1346.

Hama, H., H. Kurokawa, H. Kawano, R. Ando, T. Shimogori, H. Noda, K. Fukami, A. Sakaue-Sawano, & A. Miyawaki. 2011. "Scale: a chemical approach for fluorescence imaging and reconstruction of transparent mouse brain" [in eng]. *Nature Neuroscience* 14: 1481–8.

Hecht, E. 2015. Optics. 5th. Pearson. ISBN: 978-0-13-397722-6.

Hodge, R. D., T. E. Bakken, J. A. Miller, K. A. Smith, E. R. Barkan, L. T. Graybuck, J. L. Close, et al. 2019. "Conserved cell types with divergent features in human versus mouse cortex." *Nature* 573: 61–68.

Hörl, D., F. R. Rusak, F. Preusser, P. Tillberg, N. Randel, R. K. Chhetri, A. Cardona, et al. 2019. "BigStitcher: reconstructing high-resolution image datasets of cleared and expanded samples" [in En]. *Nature Methods* 16: 870–874.

Hou, B., D. Zhang, S. Zhao, M. Wei, Z. Yang, S. Wang, J. Wang, et al. 2015. "Scalable and DiI-compatible optical clearance of the mammalian brain" [in eng]. *Front in Neuroanatomy* 9.

Huang, S. Y., T. Witzel, B. Keil, A. Scholz, M. Davids, P. Dietz, E. Rummert, et al. 2021. "Connectome 2.0: Developing the next-generation ultra-high gradient strength human MRI scanner for bridging studies of the micro-, meso- and macro-connectome." *NeuroImage* 243: 118530.

Huisken, J., J. Swoger, F. Del Bene, J. Wittbrodt, & E. H. Stelzer. 2004. "Optical sectioning deep inside live embryos by selective plane illumination microscopy" [in eng]. *Science* 305: 1007–9.

Jacques, S. L. 2013. "Optical properties of biological tissues: a review." *Physics in Medicine & Biology* 58: R37.

Ke, M. T., S. Fujimoto, & T. Imai. 2013. "SeeDB: a simple and morphology-preserving optical clearing agent for neuronal circuit reconstruction" [in eng]. *Nat Neurosci* 16: 1154–61.

Keisuke Ota, Yasuhiro Oisi, Takayuki Suzuki, Muneki Ikeda, Yoshiki Ito, Tsubasa Ito, Kenta Kobayashi, et al. 2020. "Fast scanning high optical invariant two-photon microscopy for monitoring a large neural network activity with cellular resolution." *bioRxiv,* 2020.07.14.201699.

Kim, S. Y., J. H. Cho, E. Murray, N. Bakh, H. Choi, K. Ohn, L. Ruelas, et al. 2015. "Stochastic electrotransport selectively enhances the transport of highly electromobile molecules" [in eng]. *Proceedings of the National Academy of Sciences of the United States of America* 112: E6274–83.

Klimas, A., B. R. Gallagher, P. Wijesekara, S. Fekir, E. F. DiBernardo, Z. Cheng, D. B. Stolz, et al. 2023. "Magnify is a universal molecular anchoring strategy for expansion microscopy." *Nature Biotechnology.*

Ku, T., J. Swaney, J. Y. Park, A. Albanese, E. Murray, J. H. Cho, Y. G. Park, et al. 2016. "Multiplexed and scalable super-resolution imaging of three-dimensional protein localization in size-adjustable tissues" [in eng]. *Nat Biotechnol* 34: 973–81.

Kumar, A., Y. Wu, R. Christensen, P. Chandris, W. Gandler, E. McCreedy, A. Bokinsky, et al. 2014. "Dual-view plane illumination microscopy for rapid and spatially isotropic imaging" [in en]. *Nature Protocols* 9: 2555–2573.

Liddell, A., J. Eskesen, & N. Clack. 2025. *Acquire-zarr: Streaming directly to Zarr on the file system or cloud.*

Maitin-Shepard, J., A. Baden, W. Silversmith, E. Perlman, F. Collman, T. Blakely, J. Funke, et al. 2021. *Neuroglancer: Web-based volumetric data visualization.*

Mao, C., M. Y. Lee, J.-R. Jhan, A. R. Halpern, M. A. Woodworth, A. K. Glaser, T. J. Chozinski, et al. 2020. "Feature-rich covalent stains for super-resolution and cleared tissue fluorescence microscopy" [in en]. *Science Advances* 6: eaba4542.

McConnell, G. 2020. "Where next for the Mesolens? - 2020 - Wiley Analytical Science." *Microscopy and Analysis.*

McConnell, G., J. Trägårdh, R. Amor, J. Dempster, E. Reid, & W. B. Amos. 2016. "A novel optical microscope for imaging large embryos and tissue volumes with sub-cellular resolution throughout." *eLife* 5: e18659.

McGorty, R., H. Liu, D. Kamiyama, Z. Dong, S. Guo, & B. Huang. 2015. "Open-top selective plane illumination microscope for conventionally mounted specimens" [in EN]. *Optics Express, Vol. 23, Issue 12, pp. 16142-16153.*

Migliori, B., M. S. Datta, C. Dupre, M. C. Apak, S. Asano, R. Gao, E. S. Boyden, et al. 2018. "Light sheet theta microscopy for rapid high-resolution imaging of large biological samples" [in eng]. *BMC Biology* 16: 57.

Moore, J., C. Allan, S. Besson, J.-M. Burel, E. Diel, D. Gault, K. Kozlowski, et al. 2021. "OME-NGFF: a next-generation file format for expanding bioimaging data-access strategies." *Nature Methods* 18: 1496–1498.

Moore, J., D. Basurto-Lozada, S. Besson, J. Bogovic, E. M. Brown, J.-M. Burel, G. de Medeiros, et al. 2023. "OME-Zarr: a cloud-optimized bioimaging file format with international community support." *bioRxiv,* 2023.02.17.528834.

Narasimhan, A., K. U. Venkataraju, J. Mizrachi, D. F. Albeanu, & P. Osten. 2017. "Oblique light-sheet tomography: fast and high resolution volumetric imaging of mouse brains." *bioRxiv,* 132423.

Nogales, E., & S. H. Scheres. 2015. "Cryo-EM: A Unique Tool for the Visualization of Macromolecular Complexity." *Molecular Cell* 58: 677–689.

Oh, S. W., J. A. Harris, L. Ng, B. Winslow, N. Cain, S. Mihalas, Q. Wang, et al. 2014. "A mesoscale connectome of the mouse brain." *Nature* 508: 207–214.

Ouellette, N., A. Recknagel, K. Cao, J. Baka, M. Logsdon, & J. Chandrashekar. 2023. "Whole Mouse Brain Delipidation, Immunolabeling, and Expansion Microscopy." *protocols.io.*

Portera-Cailliau, C., R. M. Weimer, V. De Paola, P. Caroni, & K. Svoboda. 2005. "Diverse Modes of Axon Elaboration in the Developing Neocortex." *PLOS Biology* 3: e272.

Power, R. M., & J. Huisken. 2017. "A guide to light-sheet fluorescence microscopy for multiscale imaging." *Nat Meth* 14: 360–373.

Renier, N., Z. Wu, D. J. Simon, J. Yang, P. Ariel, & M. Tessier-Lavigne. 2014. "iDISCO: a simple, rapid method to immunolabel large tissue samples for volume imaging" [in eng]. *Cell* 159: 896–910.

Richardson, D. S., & J. W. Lichtman. 2015. "Clarifying Tissue Clearing" [in eng]. *Cell* 162: 246–57.

Rumyantsev, O. I., J. A. Lecoq, O. Hernandez, Y. Zhang, J. Savall, R. Chrapkiewicz, J. Li, et al. 2020. "Fundamental bounds on the fidelity of sensory cortical coding." *Nature* 580: 100–105.

Sarkar, D., J. Kang, A. T. Wassie, M. E. Schroeder, Z. Peng, T. B. Tarr, A.-H. Tang, et al. 2022. "Revealing nanostructures in brain tissue via protein decrowding by iterative expansion microscopy." *Nature Biomedical Engineering* 6: 1057–1073.

Sofroniew, N. J., D. Flickinger, J. King, & K. Svoboda. 2016. "A large field of view two-photon mesoscope with subcellular resolution for in vivo imaging." *eLife* 5: e14472.

Spalteholz, W. 1914. Über das Durchsichtigmachen von menschlichen und tierischen Präparaten und seine theoretischen Bedingungen, nebst Anhang.

Susaki, E. A., K. Tainaka, D. Perrin, F. Kishino, T. Tawara, T. M. Watanabe, C. Yokoyama, et al. 2014. "Whole-brain imaging with single-cell resolution using chemical cocktails and computational analysis" [in eng]. *Cell* 157: 726–39.

Susaki, E. A., C. Shimizu, A. Kuno, K. Tainaka, X. Li, K. Nishi, K. Morishima, et al. 2020. "Versatile whole-organ/body staining and imaging based on electrolyte-gel properties of biological tissues." *Nature Communications* 11: 1982.

Tainaka, K., S. I. Kubota, T. Q. Suyama, E. A. Susaki, D. Perrin, M. Ukai-Tadenuma, H. Ukai, & H. R. Ueda. 2014. "Whole-body imaging with single-cell resolution by tissue decolorization" [in eng]. *Cell* 159: 911–24.

Tang, L., J. Wang, J. Ding, J. Sun, X.-j. Chen, Q. Shen, R. Song, et al. 2024. "Curved light sheet microscopy for centimeter-scale cleared tissues imaging." *bioRxiv,* 2024.04.28.591483.

Tasic, B., Z. Yao, L. T. Graybuck, K. A. Smith, T. N. Nguyen, D. Bertagnolli, J. Goldy, et al. 2018. "Shared and distinct transcriptomic cell types across neocortical areas." *Nature* 563: 72–78.

Tianqi Li, Chao J. Liu, & Taner Akkin. 2019. "Contrast-enhanced serial optical coherence scanner with deep learning network reveals vasculature and white matter organization of mouse brain." *Neurophotonics* 6: 035004.

Tillberg, P. W., F. Chen, K. D. Piatkevich, Y. Zhao, C.-C. (Yu, B. P. English, L. Gao, et al. 2016. "Protein-retention expansion microscopy of cells and tissues labeled using standard fluorescent proteins and antibodies." *Nature Biotechnology* 34: 987–992.

Tillberg, P. W., & F. Chen. 2019. "Expansion Microscopy: Scalable and Convenient Super-Resolution Microscopy." *Annual Review of Cell and Developmental Biology* 35: 683–701.

Tomer, R., L. Ye, B. Hsueh, & K. Deisseroth. 2014. "Advanced CLARITY for rapid and high-resolution imaging of intact tissues" [in eng]. *Nature Protocols* 9: 1682–97.

Tomer, R., K. Khairy, F. Amat, & P. J. Keller. 2012. "Quantitative high-speed imaging of entire developing embryos with simultaneous multiview light-sheet microscopy" [in En]. *Nature Methods* 9: 755.

Truckenbrodt, S., M. Maidorn, D. Crzan, H. Wildhagen, S. Kabatas, & S. O. Rizzoli. 2018. "X10 expansion microscopy enables 25-nm resolution on conventional microscopes." *EMBO reports* 19: e45836.

Tsai, P. S., J. P. Kaufhold, P. Blinder, B. Friedman, P. J. Drew, H. J. Karten, P. D. Lyden, & D. Kleinfeld. 2009. "Correlations of neuronal and microvascular densities in murine cortex revealed by direct counting and colocalization of nuclei and vessels" [in eng]. *J Neurosci* 29: 14553–70.

Van Essen, D. C., C. J. Donahue, T. S. Coalson, H. Kennedy, T. Hayashi, & M. F. Glasser. 2019. "Cerebral cortical folding, parcellation, and connectivity in humans, nonhuman primates, and mice." *Proceedings of the National Academy of Sciences* 116: 26173–26180.

Vladimirov, N., F. F. Voigt, T. Naert, G. R. Araujo, R. Cai, A. M. Reuss, S. Zhao, et al. 2024. "Benchtop mesoSPIM: a next-generation open-source light-sheet microscope for cleared samples." *Nature Communications* 15: 2679.

Voigt, F. F., D. Kirschenbaum, E. Platonova, S. Pagès, R. A. A. Campbell, R. Kastli, M. Schaettin, et al. 2019. "The mesoSPIM initiative: open-source light-sheet microscopes for imaging cleared tissue" [in En]. *Nature Methods* 16: 1105–1108.

Voigt, F. F., A. M. Reuss, T. Naert, S. Hildebrand, M. Schaettin, A. L. Hotz, L. Whitehead, et al. 2024. "Reflective multi-immersion microscope objectives inspired by the Schmidt telescope." *Nature Biotechnology* 42: 65–71.

Voleti, V., K. B. Patel, W. Li, C. P. Campos, S. Bharadwaj, H. Yu, C. Ford, et al. 2019. "Real-time volumetric microscopy of in vivo dynamics and large-scale samples with SCAPE 2.0" [in En]. *Nature Methods* 16: 1054–1062.

Wang, X., H. Xiong, Y. Liu, T. Yang, A. Li, F. Huang, F. Yin, et al. 2021. "Chemical sectioning fluorescence tomography: high-throughput, high-contrast, multicolor, whole-brain imaging at subcellular resolution." *Cell Reports* 34: 108709.

Weiss, K. R., F. F. Voigt, D. P. Shepherd, & J. Huisken. 2021. "Tutorial: practical considerations for tissue clearing and imaging." *Nature Protocols* 16: 2732–2748.

Winnubst, J., E. Bas, T. A. Ferreira, Z. Wu, M. N. Economo, P. Edson, B. J. Arthur, et al. 2019. "Reconstruction of 1,000 Projection Neurons Reveals New Cell Types and Organization of Long-Range Connectivity in the Mouse Brain." *Cell* 179: 268–281.e13.

Wu, Y., P. Wawrzusin, J. Senseney, R. S. Fischer, R. Christensen, A. Santella, A. G. York, et al. 2013. "Spatially isotropic four-dimensional imaging with dual-view plane illumination microscopy" [in English]. *Nat Biotechnol.*

Xiaoli Qi, Rodrigo Muñoz-Castañeda, Arun Narasimhan, Liya Ding, Xin Chen, Corey Elowsky, Jason Palmer, et al. 2023. "High-throughput confocal airy beam oblique light-sheet tomography of brain-wide imaging at single-cell resolution." *bioRxiv,* 2023.06.04.543586.

Xu, F., Y. Shen, L. Ding, C.-Y. Yang, H. Tan, H. Wang, Q. Zhu, et al. 2021. "High-throughput mapping of a whole rhesus monkey brain at micrometer resolution." *Nature Biotechnology* 39: 1521–1528.

Yang, B., J. B. Treweek, R. P. Kulkarni, B. E. Deverman, C. K. Chen, E. Lubeck, S. Shah, L. Cai, & V. Gradinaru. 2014. "Single-cell phenotyping within transparent intact tissue through whole-body clearing" [in eng]. *Cell* 158: 945–958.

Yi Cui, Gaojie Yang, Daniel R. Goodwin, Ciara H. O'Flanagan, Anubhav Sinha, Chi Zhang, Kristina E. Kitko, et al. 2022. "A Multifunctional Anchor for Multimodal Expansion Microscopy." *bioRxiv,* 2022.06.19.496699.

Yu, C.-H., J. N. Stirman, Y. Yu, R. Hira, & S. L. Smith. 2021. "Diesel2p mesoscope with dual independent scan engines for flexible capture of dynamics in distributed neural circuitry." *Nature Communications* 12: 6639.

Yu, C.-H., Y. Yu, L. M. Adsit, J. T. Chang, J. Barchini, A. H. Moberly, H. Benisty, et al. 2024. "The Cousa objective: a long-working distance air objective for multiphoton imaging in vivo." *Nature Methods* 21: 132–141.

Yueqian, Z., & G. Herbert. 2019. "Systematic design of microscope objectives. Part I: System review and analysis" [in English]. *Advanced Optical Technologies* 8: 313–347.

Zhang, Y., & H. Gross. 2019. "Systematic design of microscope objectives. Part II: Lens modules and design principles," Advanced Optical Technologies, 8: 349–384.

Zhang, Z., X. Yao, X. Yin, Z. Ding, T. Huang, Y. Huo, R. Ji, H. Peng, & Z. V. Guo. 2021. "Multi-Scale Light-Sheet Fluorescence Microscopy for Fast Whole Brain Imaging." *Frontiers in Neuroanatomy* 15.

Zizhen Yao, Cindy T. J. van Velthoven, Michael Kunst, Meng Zhang, Delissa McMillen, Changkyu Lee, Won Jung, et al. 2023. "A high-resolution transcriptomic and spatial atlas of cell types in the whole mouse brain." *bioRxiv,* 2023.03.06.531121.

Supplementary Material

Note S1. Comparisons of theoretical camera sensitivity and speed.

Unlike existing SPIM systems, the ExA-SPIM system uses the large-format SONY IMX411 CMOS sensor with different specifications from sCMOS cameras. With respect to sensitivity, the read noise is the most important specification. While the read noise is ~1 *e*- for a sCMOS camera, it is 6.89, 4.57, and 3.48 *e*- for 12, 14, and 16-bit readout modes for the SONY IMX411 sensor. The signal-to-noise ratio (SNR) of a camera sensor can be calculated as:

$$SNR = \frac{QE \times S}{\sqrt{QE \times (S + B) + R^2}} \tag{2}$$

where, QE is the quantum efficiency of the sensor, S is the signal in photons, B is the background signal in photons, and R is the readout noise in *e*-. Plots for a sCMOS and the Sony IMX411 sensor are shown in **Figure S8**. These plots yield insights into for an equivalent number of photons, how the SNR of the sensors would differ, or how many photons each sensor would require to achieve the same SNR. In general, the sCMOS provides much greater SNR at low-light levels (i.e. <50 photons), with diminishing benefits for higher photon levels, especially when compared to the 14, and 16-bit modes of the SONY IMX411 sensor. However, it is also important to consider the SNR as a function of the imaging speed (i.e., pixels/sec) of the sensor (**Figure 2e**). For example, when operated with 14-bit readout, the line time of the Sony IMX411 sensor is 20.15 μs. With 14192 pixels per row on the sensor, this corresponds to an imaging speed of 703×10^6 voxels/sec. This contrasts with a traditional sCMOS sensor that only contains 2048 pixels per row, where even at the fastest 4.89 μs line time, the imaging speed is only 418×10^6 voxels/sec. In other words, the Sony IMX411 sensor provides more pixel parallelization within each row. This enables twice the voxel rate with four times the pixel dwell time (i.e., four times the collected signal). It is important to note that sCMOS sensors provide a direct adjustment of the sensor line time, to precisely trade-off between sensitivity and imaging speed. For the Sony IMX411 sensor, the line time can be indirectly adjusted by setting the maximum data bandwidth of the camera's data stream. For example, for 16-bit data over entire 14192×10640 frames, the line time could be set to 100 μs by setting the bandwidth to 284 MB/sec.

Table S1: Summary of custom lenses for fluorescence microscopy.

Reference	Name	Liquid immersion	*f*	NA	Field of view	Etendue	Working distance
(Tang et al. 2024)	Curved LSFM	1.33 - 1.56	118	0.25	13.00	8.30	20.00
(Current study)	ExA-SPIM	1.33 - 1.56	100	0.31	16.40	19.65	40.00
(Fan et al. 2019)	RUSH	-	-	0.35	14.00	18.86	19.00
(Keisuke Ota et al. 2020)	FASHIO-2PM	-	35	0.40	4.24	2.26	4.50
(McConnell et al. 2016)	Mesolens	1.33 - 1.56	50	0.47	6.00	1.13	3.00
(Yu et al. 2024)	Cousa	-	20	0.50	2.00	0.79	20.00
(Yu et al. 2021)	Diesel2P	-	30	0.54	6.00	8.24	8.00
(Kyocera)	CS06-10-40-154	1.52 - 1.56	18	0.60	2.00	1.13	40.60
(Sofroniew et al. 2016)	2p-RAM	-	21	0.60	5.00	7.07	2.70
(Voigt et al. 2024)	Schmidt	1.33 - 1.56	-	1.00	1.15	1.04	11.00

Units
f - mm
field of view - mm
etendue - mm^2
working distance - mm

Table S2: Comparison of large-scale volumetric imaging modalities.

Reference	Imaging method	Optical resolution	Voxel size	Isotropy	Focal volume	Voxel rate
(Economo et al. 2016)	2p tomography	0.45×0.45×1.33	0.30×0.30×1.00	2.96:1	0.27	16
(Gong et al. 2016)	fMOST	0.32×0.32×2.00	0.32×0.32×2.00	6.25:1	0.20	4
(Narasimhan et al. 2017)	Oblique light-sheet	0.75×0.75×6.90	0.41×0.41×0.41	9.20:1	3.88	419
(Migliori et al. 2018)	Light-sheet theta	0.34×0.34×3.00	0.23×0.23×5.00	8.82:1	0.29	105
(Chakraborty et al. 2019)	Axially-swept SPIM	0.48×0.48×0.48	0.16×0.16×0.16	1:1	0.11	42
(Voleti et al. 2019)	SCAPE 2.0	0.60×1.21×1.55	0.24×0.24×0.24	2.58:1	1.13	419
(R. Gao et al. 2019)	ExLLSM	0.06×0.06×0.09	0.03×0.03×0.04	1.5:1	«0.01	68
(D. Chen et al. 2020)	Multifocal 2p tomography	0.36×0.36×2.59	0.40×0.40×1.00	7.19:1	0.34	77
(Guo et al. 2020)	Dual-inverted SPIM	0.48×0.48×0.48	0.24×0.24×0.24	1:1	0.11	419
(Y. Chen et al. 2020)	Tiling SPIM	0.30×0.30×2.50	0.30×0.30×1.50	5:1	0.22	105
(Wang et al. 2021)	fMOST	0.34×0.34×2.00	0.23×0.23×1.00	5.88:1	0.23	136
(Zhang et al. 2021)	Axially-swept SPIM	0.95×0.95×2.10	0.52×0.52×1.00	2.21:1	1.90	84
(Xu et al. 2021)	VISOR2 SPIM	1.00×1.00×2.50	1.00×1.00×2.50	2.5:1	2.50	373
(Glaser et al. 2022)	Open-top light-sheet	0.45×0.45×2.91	0.20×0.20×0.20	6.47:1	0.59	105
(Xiaoli Qi et al. 2023)	Confocal airy light-sheet	0.76×0.76×2.20	0.26×0.26×1.06	2.08:1	1.27	419
(Vladimirov et al. 2024)	Benchtop mesoSPIM	1.50×1.50×3.30	0.75×0.75×2.00	2.2:1	7.43	37
(Tang et al. 2024)	Curved LSFM	1.22×1.22×2.50	0.63×0.63×1.25	2:1	3.72	130
(Current study)	ExA-SPIM (1×)	1.00×1.00×3.00	0.75×0.75×1.00	3:1	6.75	725
(Current study)	ExA-SPIM (2×)	0.50×0.50×1.50	0.38×0.38×0.50	3:1	0.84	725
(Current study)	ExA-SPIM (3×)	0.33×0.33×1.00	0.25×0.25×0.33	3:1	0.25	725
(Current study)	ExA-SPIM (4×)	0.25×0.25×0.75	0.19×0.19×0.25	3:1	0.11	725

Units
optical resolution - µm
voxel size - µm
focal volume - μm^3
voxel rate - megavoxels/sec

Note, only modalities capable of providing $\leq$1.5 µm lateral optical resolution are included.

Table S3: ExA-SPIM imaging across scales.

Manufacturer	Model	Magnification	NA	Lateral resolution	Field of view	Etendue	Speed
Schneider-Kreuznach	VEO_JM DIAMOND 1.43×/F3.0	1.43	0.10	3.05	57.34	26.34	2137
Schneider-Kreuznach	VEO_JM DIAMOND 1.67×/F3.0	1.67	0.10	3.05	49.10	19.32	1340
Schneider-Kreuznach	VEO_JM DIAMOND 2.5×/F2.6	2.50	0.13	2.35	32.80	15.17	400
Schneider-Kreuznach	VEO_JM DIAMOND 3.33×/F2.1	3.33	0.18	1.69	24.62	15.43	170
Schneider-Kreuznach	VEO_JM DIAMOND 5.0×/F1.3	5.00	0.31	1.00	16.40	19.65	50
Nikon	Rayfact 1.4S	1.40	0.11	2.77	61.71	36.19	2277
Nikon	Rayfact 1.7S	1.70	0.11	2.77	49.37	23.16	1272
Nikon	Rayfact 2.5S	2.50	0.14	2.18	34.56	18.39	400
Nikon	Rayfact 3.5S	3.50	0.16	1.91	24.69	12.25	146
Nikon	Rayfact 5S	5.00	0.17	1.79	17.28	6.78	50
Nikon	Rayfact 1-2x Variable Lens	1.00	0.09	3.39	86.4	47.49	6249
Nikon	Rayfact 1-2x Variable Lens	2.00	0.12	2.54	43.2	21.11	781
Nikon	Rayfact 2-5x Variable Lens	2.00	0.13	2.35	43.2	24.77	781
Nikon	Rayfact 2-5x Variable Lens	5.00	0.17	1.79	16.6	6.25	50

Units
lateral resolution - µm
field of view - mm
etendue - mm^2
speed - cm^3 per day

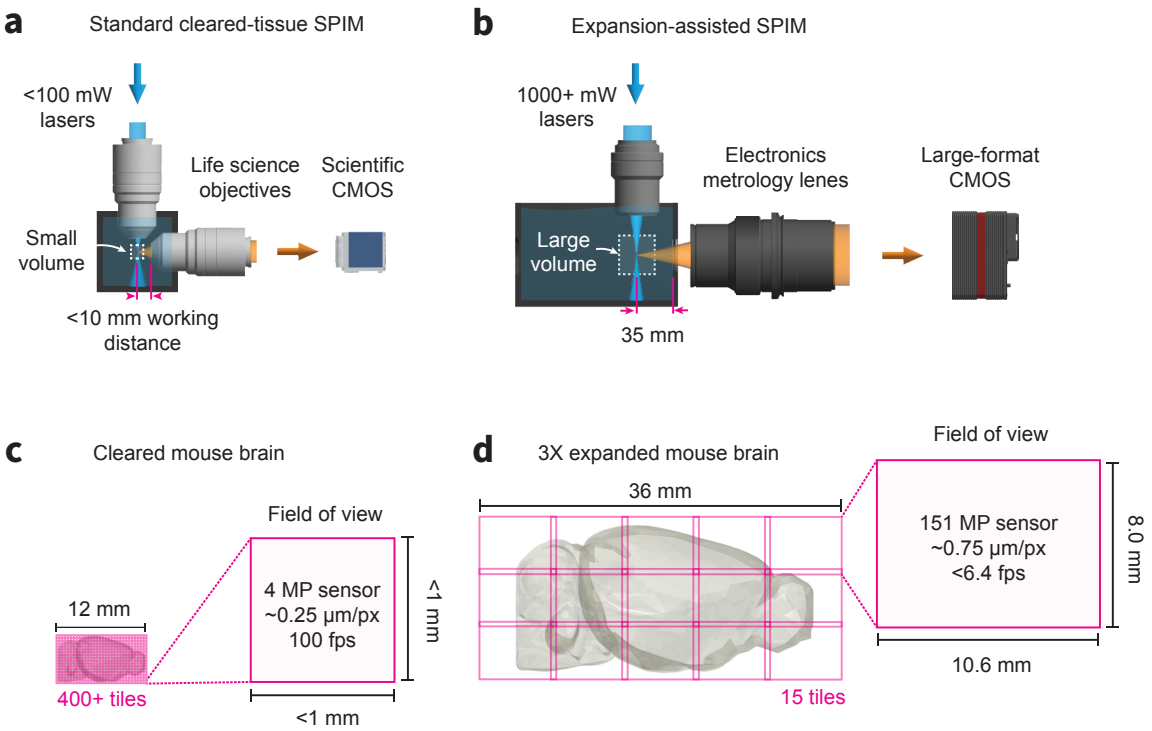

Figure S1: Comparison between standard cleared-tissue and expansion-assisted SPIM. (a-c) A traditional cleared-tissue SPIM system uses standard 100 mW or less lasers, a scientific CMOS camera, and life sciences objectives with higher NA and <10 mm working distance. In theory, these systems can image an entire cleared mouse brain at 500 nm or less resolution without any physical cutting. However, this would require 400+ individual image tiles, and high camera framerates which is problematic for techniques such as axial sweeping. **(b-d)** By comparison, the ExA-SPIM system uses 1000+ mW lasers, a large-format CMOS camera, and electronics metrology lenses with a moderate NA and ~35 mm working distance. After expanded a mouse brain 3×, the system is still capable of imaging the entire brain in only 15 tiles.

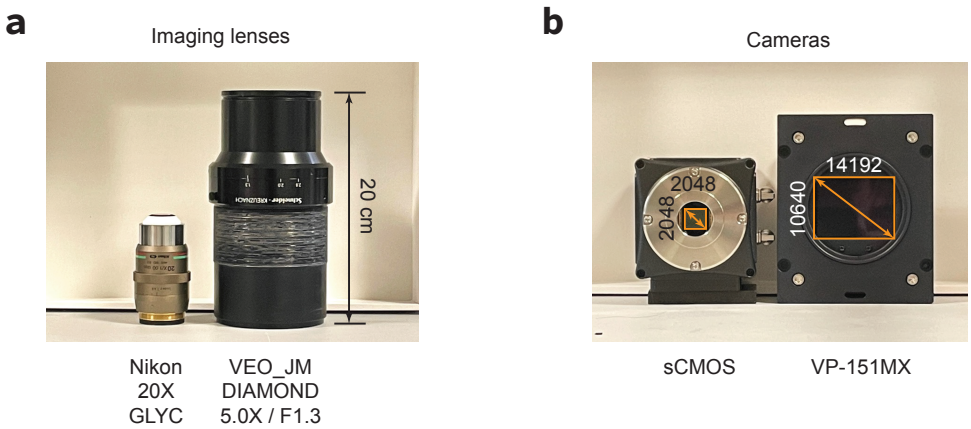

Figure S2: Comparison of electronics metrology and life sciences technologies for large-scale volumetric imaging. **(a)** Nikon 20× GLYC next to the VEO_JM DIAMOND 5.0× / F1.3 lens. **(b)** Traditional sCMOS camera with 2048×2048 pixels next to the VP-151MX camera with the Sony IMX411 sensor with 14192×10640 pixels.

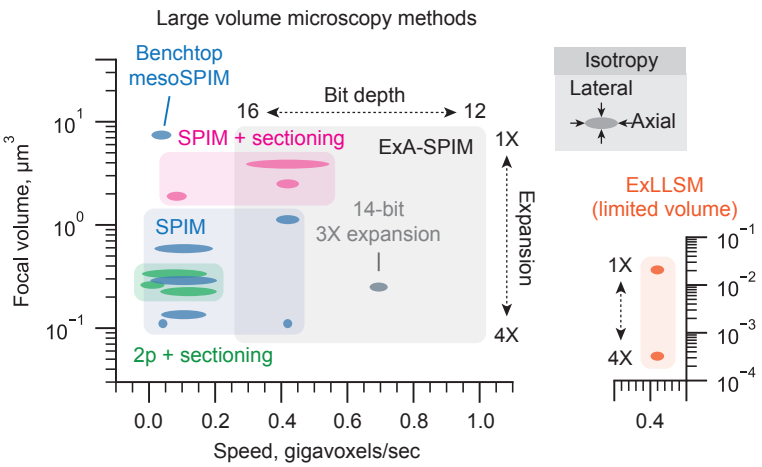

Figure S3: Comparison of methods for large-scale volumetric imaging. Summary plot comparing the resolution, isotropy, and imaging speed of various existing large volume microscopy methods (2p and SPIM). Methods that do or do not use sectioning are highlighted. The aspect ratio of each marker indicates the relative isotropy of the method. Note that expansion lattice light-sheet microscopy (ExLLSM) (G. Gao et al. 2023) is capable of a very small effective focal volume but over very limited volumes (« 1 mm^3) and is shown in a dedicated inset. The Benchtop mesoSPIM system (Vladimirov et al. 2024), which sits outside of the other SPIM systems is highlighted.

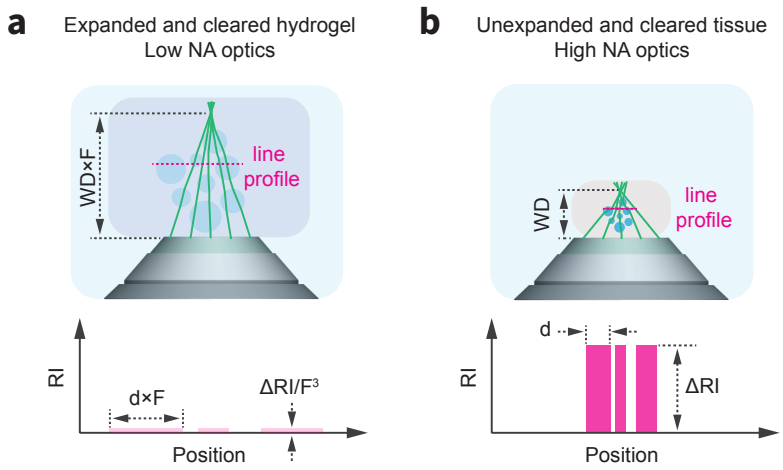

Figure S4: Comparing expansion-assisted versus cleared-tissue imaging. Although clearing and expansion protocols render tissues transparent, there still exist small refractive index inhomogeneities, ΔRI, which degrade image quality at larger imaging depths. This effect is more extreme for high NA lenses, as light enters the objective over a larger collection angle, leading to path differences between extreme and axial rays (i.e. wavefront error). This effect is reduced for low NA optics. In addition, when tissues are expanded by a factor, F, the refractive index inhomogeneities reduce to the third power, while the imaging path length through tissue, WD, only increases to the first power. The reduced aberration sensitivity of low NA optics, combined with the increased homogenization of refractive index through the expansion process explain, in part, the benefits of expansion-assisted imaging.

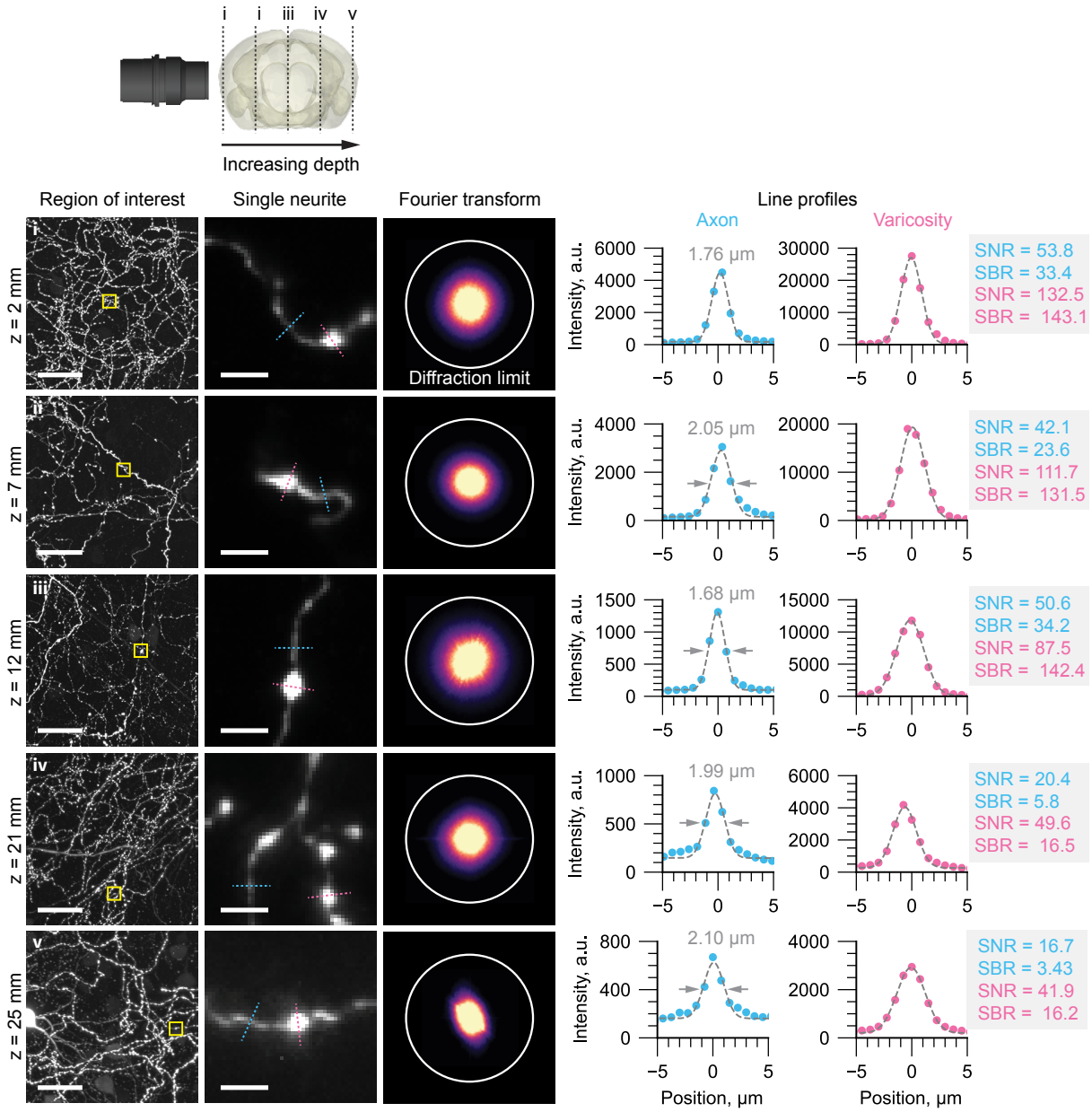

Figure S5: Image quality versus imaging depth. Representative regions of interest of individual axons in a mouse brain are shown at increasing imaging depths. At each imaging depth, the Fourier transform is shown with a circle denoting the expected diffraction-limited resolution of the microscope. Line profiles through individual axons and varicosities are also shown, with the full-width-half-maximum, signal-to-noise-ratio (SNR), and signal-to-background-ratio (SBR) estimated. The *SNR* was calculated assuming shot noise limited detection:

$$SNR = \sqrt{P}$$

where *P* (photons) was calculated by converting the arbitrary intensity units (a.u.) to photons using the gain factor, *K* (*e*-/a.u.) and quantum efficiency, *QE* (*e*-/photon) of the camera sensor.

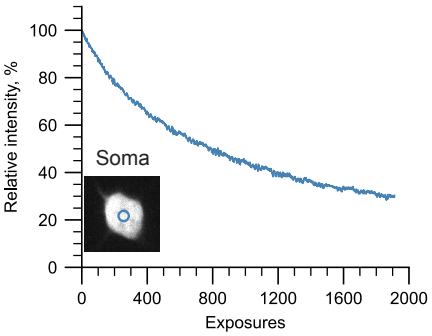

Figure S6: Photobleaching at high excitation laser powers. The same region in an expanded mouse brain sample was irradiated repeatedly to measure photobleaching at the excitation powers used by the ExA-SPIM. Decay curves for a soma (blue) was measured over 2000 repeated exposures. Because the higher excitation power of the ExA-SPIM is distributed over an 11 mm wide light sheet, the light intensity is similar to typical standard SPIM (10^5 - 10^6 mW/cm^2). Only modest photobleaching was observed (~50% reduction in intensity after ~800 exposures.

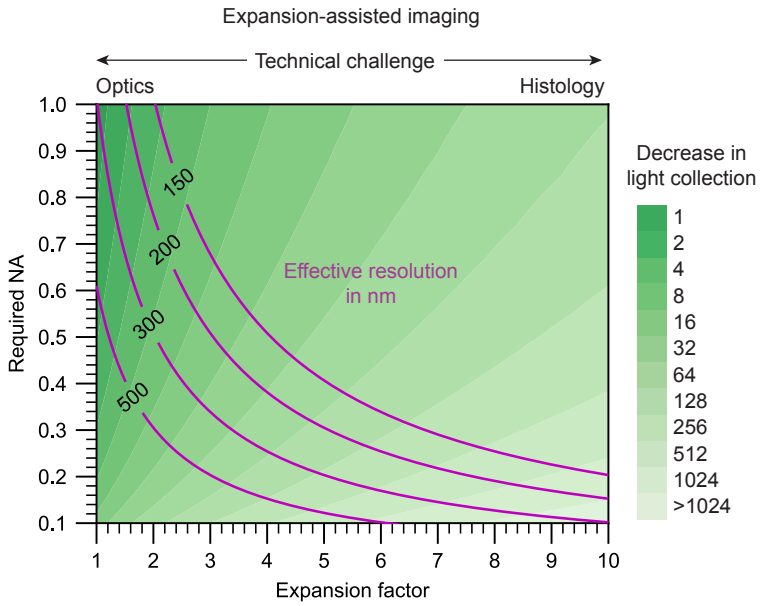

Figure S7: Factors to consider for expansion-assisted imaging. A continuum of NA and expansion factor combinations can achieve a desired effective resolution. Light collection efficiency (which decreases quadratically with NA) and required working distance (which increases linearly with expansion factor) should be considered when deciding on exact parameters to use for expansion-assisted imaging.

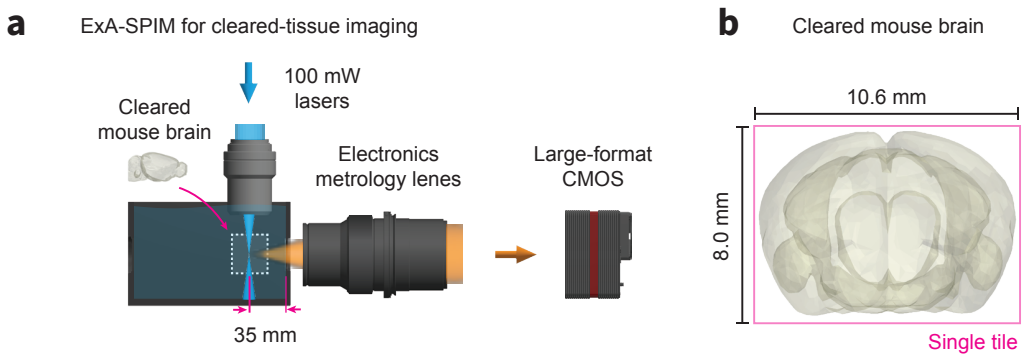

Figure S8: Cleared-tissue imaging with the ExA-SPIM system. **(a)** Although we have focused on imaging expanded tissues, the ExA-SPIM microscope does not require expansion. The chamber can be filled with any refractive-index matching media, and the liquid working distance of the electronics metrology lens can be adjusted slightly to recover diffraction-limited imaging performance. **(b)** As an example, an entire cleared mouse brain could be imaged coronally in a single tile.

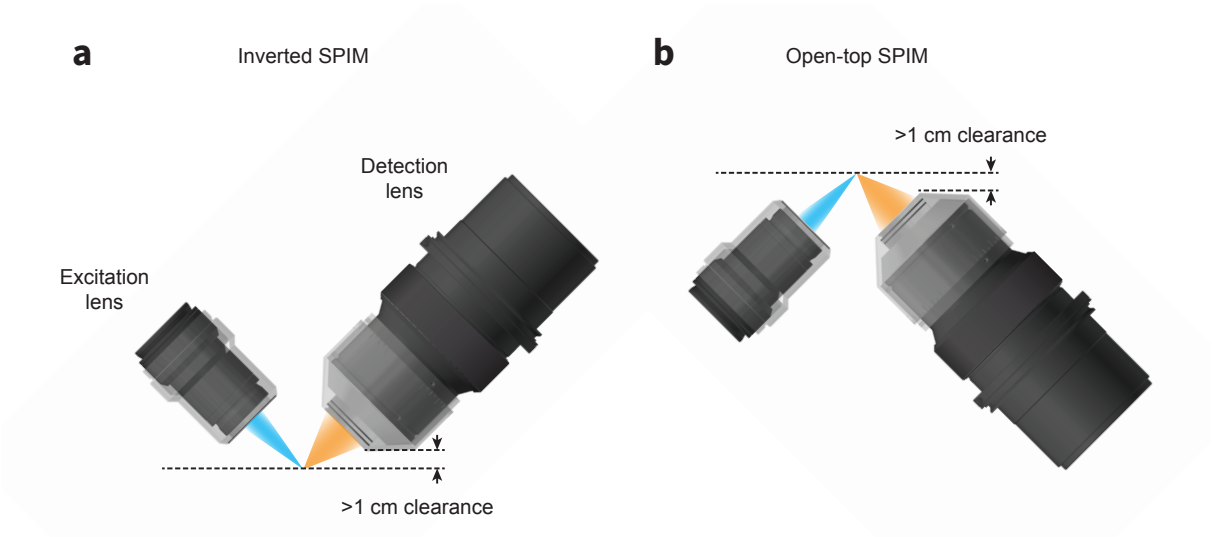

Figure S9: Inverted and open-top ExA-SPIM designs. Schematics for configuring the ExA-SPIM system in an **(a)** inverted or **(b)** open-top architecture. In both geometries, the working distance and mechanical housing of the lenses provides >1 cm of clearance, enabling imaging large tissue sections up to 1 cm thick. This geometry also reduces pathlengths through the tissue, reducing the demands on optical clearing and tissue clarity.

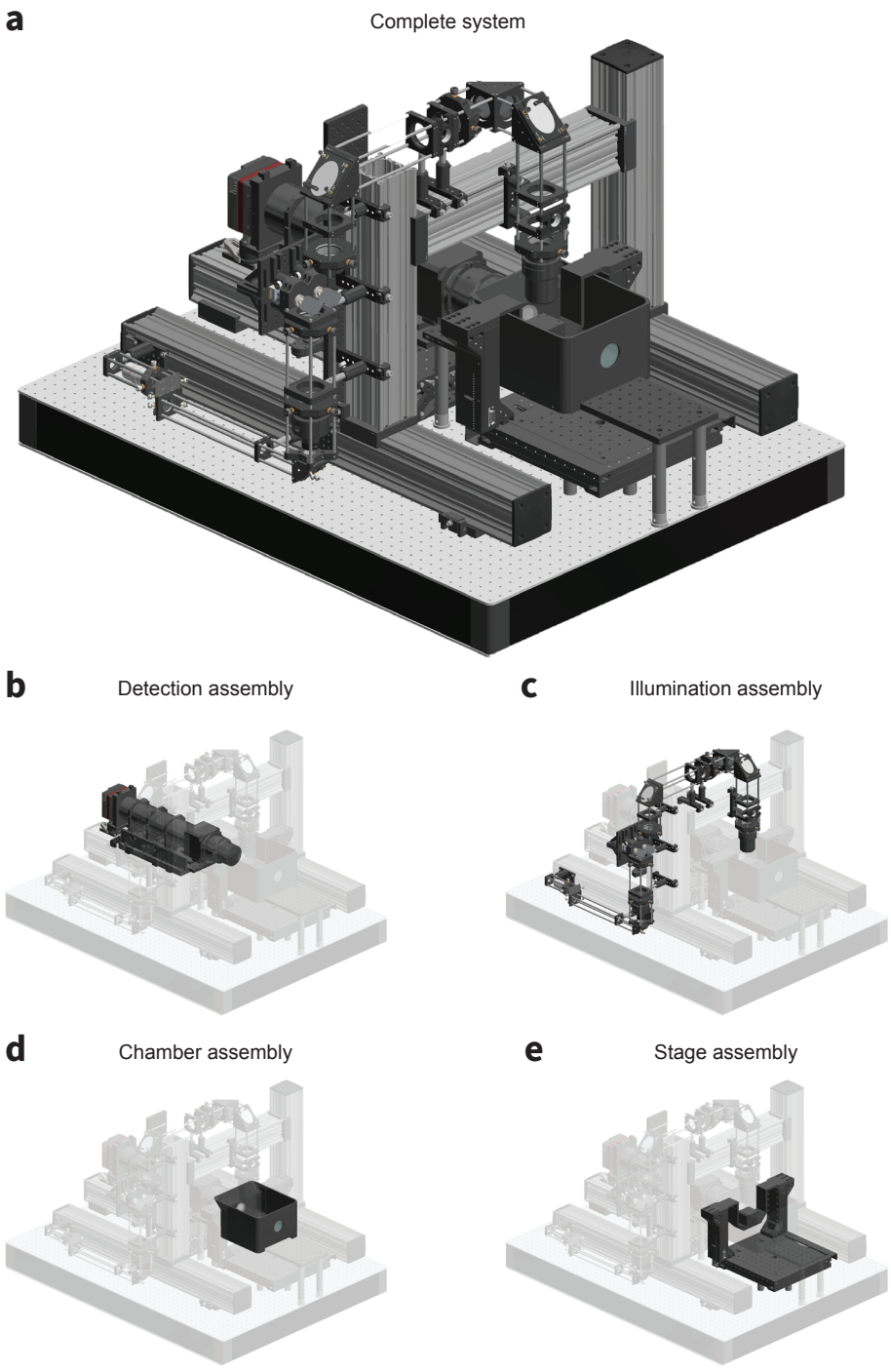

Figure S10: ExA-SPIM mechanical layout. CAD renderings of the microscope detailing **(a)** the complete system, **(b)** the detection assembly, **(c)** the illumination assembly, **(d)** the chamber assembly, and **(e)** the stage assembly.

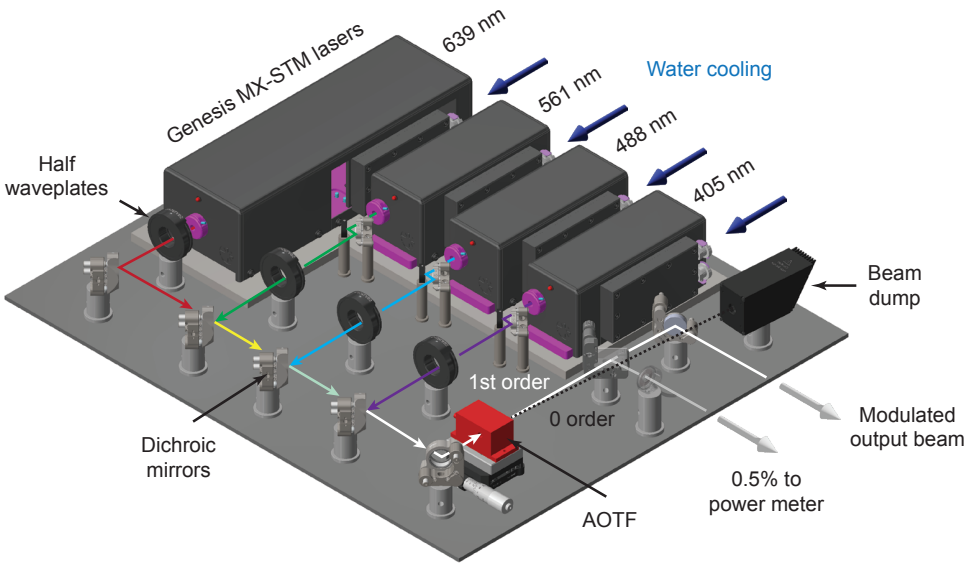

Figure S11: ExA-SPIM laser combiner. The system uses three 1000 mW lasers at 488, 561, and 639 nm (Genesis MX-STM series, Coherent) with an optional 405 nm laser. The beam from each laser (~1 mm in diameter) first passes through a half waveplate for polarization rotation. The beams are all then combined using a series of dichroic mirrors mounted in kinematic mounts. An acousto-optic tunable filter (AOTF) is used to both select wavelength and modulate the power of each laser. The 0-order beam from the AOTF terminates in a beam dump, whereas the modulated 1st order beam is reflected off a final kinematic mirror before being injected into the microscope. An AR coated glass plate is used to reflect ~0.5% of the output beam to a power meter for monitoring during dataset acquisition.

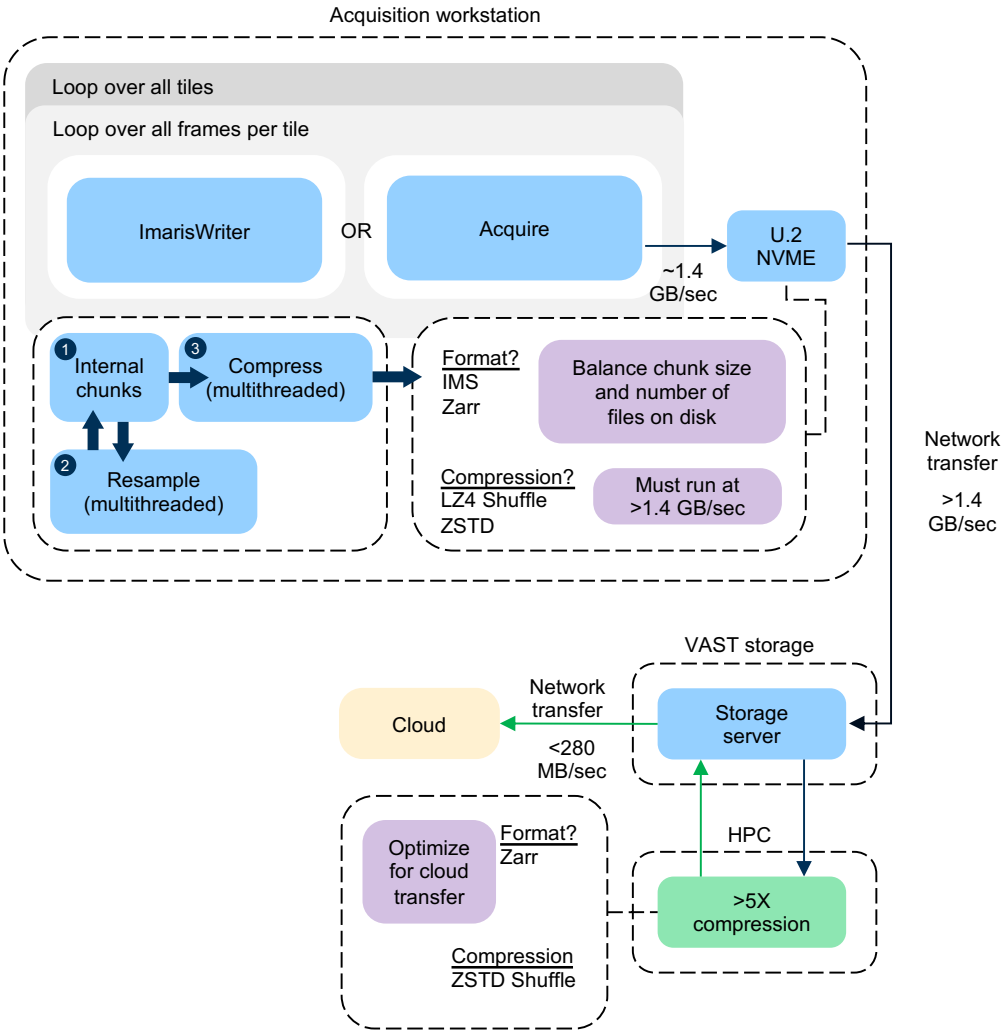

Figure S12: ExA-SPIM image acquisition scheme. A block diagram summarizing the acquisition procedure for an ExA-SPIM dataset is shown. Each dataset requires looping over the total frames within a given tile, and then all tiles within a given dataset. Each tile results in a single file on disk, which is copied over the network to a local VAST storage system. The transfer of the previous tile occurs synchronously with the acquisition of the next tile, and the transfer speed to the VAST system outpaces the data generation speed of the microscope. For the ImarisWriter workflow, once tiles are transferred to the VAST storage system, they are synchronously converted to OME-Zarr files with ZSTD Shuffle compression. After compression, the files are written directly to cloud storage. The compression and conversion to OME-Zarr also runs at a speed which outpaces the microscope.

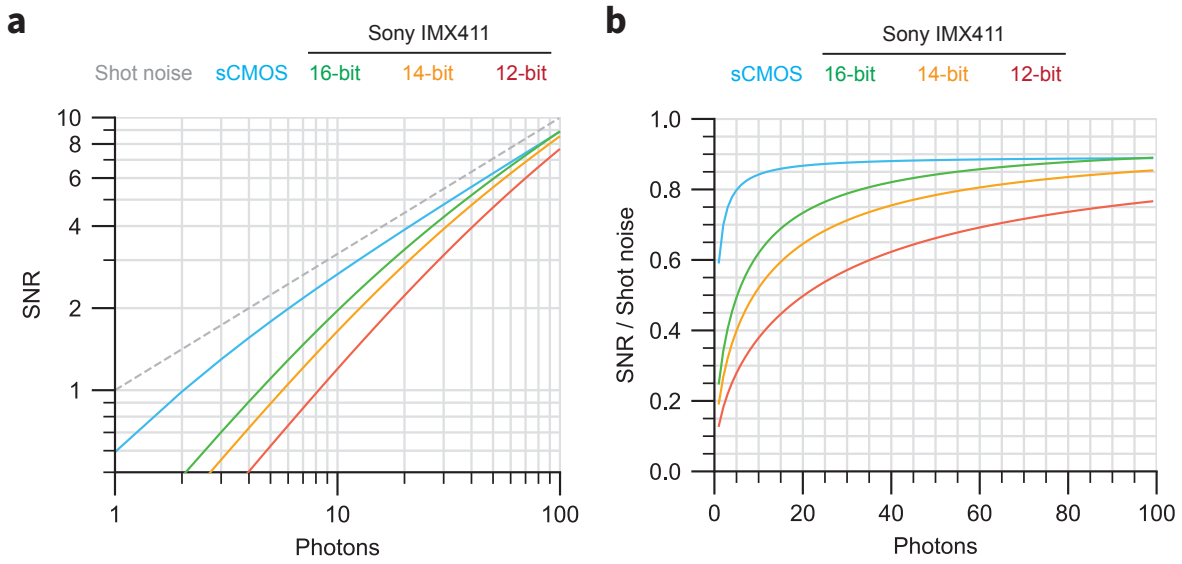

Figure S13: Simulations of camera sensitivity. (a) Simulations of SNR versus collected photons for sCMOS (cyan) and the Sony IMX411 sensor with 16-bit (green), 14-bit (yellow), and 12-bit (red) readout. The SNR for an ideal perfect sensor is highlighted. **(b)** Relative SNR values for the curves shown in **(a)**, normalized to the ideal sensor curve.